Three-dimensional structure of cold-water gravity currents

N. Castro-Folker,[1,*] A. P. Grace,[2] and M. Stastna[1]
[1]*Department of Applied Mathematics, University of Waterloo, Waterloo, Canada N2L 3G1*
[2]*Department of Civil and Environmental Engineering and Earth Sciences, University of Notre Dame, Notre Dame, Indiana 46556, USA*

(Received 25 July 2023; accepted 2 October 2023; published 6 November 2023)

Counterintuitively, fresh water attains a maximum density at a temperature above its freezing point. As a result, it exhibits a phenomenon known as weak cabbeling. If a system is in the weak cabbeling regime, then the mean density of the system is not equal to the density evaluated at the mean temperature. The dynamics of freshwater gravity currents are known to be influenced by weak cabbeling, but research on this influence has been restricted to two-dimensional systems with stress-free (free-slip) boundaries. We extend this work by simulating pairs of three-dimensional systems in the weak cabbeling regime with no-slip conditions imposed on the vertical boundaries. In each pair, we have a floating and sinking current: The former has a cold current intruding into a system at the temperature of maximum density, and the latter has the reverse. We define currents that form such a pair to be *conjugate*. The initial shape and size of conjugate currents are the same, so we would expect the distribution of the intruding fluid to evolve identically under the change of coordinates $(y, z) \to (L_y - y, L_z - z)$, where L_y is the domain width and L_z is the domain height. This symmetry is broken two dimensions when a nonlinear equation of state is assumed; we will show that this result extends to three dimensions. We will report on differences among the lobe-cleft instability, the shear instability, the mixing, and the bed-stresses of three-dimensional conjugate currents. Curiously, we observe that differences in the lobe-cleft instability manifest only after secondary instabilities develop. We also identify and discuss structures created by the lobe-cleft instability that, to our knowledge, have been under-reported in the literature.

DOI: 10.1103/PhysRevFluids.8.113901

I. INTRODUCTION

Gravity currents are horizontal intrusions driven by a density difference between the intruding and ambient fluid. When the current is lighter than the ambient fluid it is said to be hypopycnal, and when it is denser it is said to be hyperpycnal. Gravity currents are ubiquitous in nature [1–3], with rivers emptying into estuaries [4], the flow of one sea into another [5], the spread of storm clouds [6], and volcanic discharge [7] all being examples of geophysical gravity currents. Early theoretical investigations into gravity currents were concerned with self-similar solutions of inviscid systems [3,8,9]. Subsequent experimental research of gravity currents was therefore concerned with with measuring the height and speed of gravity currents and analyzing the data through the lens of the. idealized, self-similar solutions [3,10–13]. Of course, the effects of friction along the density interface and along the boundaries led to observed deviations from the theory [10–13]. The most notable effects of friction are the production of coherent structures below, above, and behind the current head [10].

*ncastrof@uwaterloo.ca

Laboratory and field investigations also reported on three-dimensional coherent structures near and below the nose of a gravity current, which are understood to be the result of the lobe-cleft instability [10,11,14–16]. Simpson [10] described these instabilities as "projecting noses with bulges or buttresses," and Ellison [14] noted that they cause the front to appear as if it "advances in a series of localized bursts." Härtel *et al.* [15,17] performed a stability analysis and direct numerical simulation (DNS) of Boussinesq gravity currents that undergo a lobe-cleft instability. As prior investigations determined the lobe-cleft instability is suppressed in the presence of free-slip boundary conditions [10], the stability analysis assumes no-slip boundary conditions. Consistent with results from laboratory experiments, this analysis showed that spanwise-varying perturbations to the velocity and density fields due to the lobe-cleft instability grow near the front and bottom of the current head; the authors also showed that the wavelength of the fastest growing mode decreases with Gr, a dimensionless number that measures the scale of the buoyancy force relative to viscous forces [15]. Experiments and three-dimensional DNS of no-slip gravity currents demonstrate that the lobes continually change in shape and size, with a lobe splitting into two, or two lobes merging into one [10,16–20]. Simulations show that the interface of high-Gr Boussinesq gravity currents are populated by (baroclinic) hairpin vortices [20], and it is proposed that the merging and splitting process is due to the interactions of those vortices near the front of the current [16]. Similarly, the effects on vorticity of surface tension in viscous gravity currents [21], and of particle diameter in non-Boussinesq sediment-laden currents [22], are thought to modulate the evolution of lobe-cleft structures.

The billows, lobes, and clefts are of interest not just because they present a significant deviation from the inviscid theory, but because they also play an integral role in the transport of heat and mass in a myriad of geophysical settings [3,5,23–25]. The review articles by Meiburg and Kneller [23], and Wells and Dorrell [25] outline how turbidity currents generated near the shores of lakes and coastal oceans are affected by the instabilities and their resultant coherent structures. According to Wells and Dorrell [25], these turbidity currents are generated by either sediment-laden outflow from rivers or subsurface landslides and can travel large distances along the bed. Turbidity currents have large values of turbulent kinetic energy (TKE) near the front and bottom of the current interface [26]. The largest values of TKE are found in the wake along the top of the current, where eddies induced by the shear-instability entrain the ambient fluid [26]. The high-TKE, turbulent flow along the bottom of the current also generates sufficient stress to scour and erode sediment along the bottom boundary. Indeed, large-eddy simulations of high-Gr hyperpycnal currents show that the turbulent wake of a gravity current entrains fluid from the upper water column while the lobe-cleft structures entrain fluid from the bottom boundary layer [27]. If a turbidity current encounters a flat topography, then it will eventually be extinguished, as friction along the boundary slows the current by direct and indirect mechanisms [28]. The direct mechanism is somewhat obvious, since friction decreases the TKE of the current; but, this decrease in TKE also causes sediment to precipitate from the current, which gradually decreases the density difference between the intruding and ambient fluid [20]. Indeed, the wavelike shape of turbidites—minerals formed by accumulated ancient sediment—are believed to be influenced by the lobes and clefts at the front of the decaying gravity currents that transported the sediment to its ultimate destination [28,29].

In lakes during winter, gravity currents are not necessarily turbid and can be generated by temperature differences alone [30]. During the freezing/thawing of winter lakes, nonuniform bathymetry results in horizontal density gradients which can generate fresh-water gravity currents [30–33]. In the middle of winter, when solar radiation cannot penetrate the surface ice, heat retained by sediment can warm near-freezing water to the temperature of maximum density, which results in hyperpycnal gravity currents [30]. The circulation induced by these currents are integral to hydrological and biological processes during the deep winter [30,31,34]. Temperature-driven density differences in cold water are especially interesting, as the density attains a maximum value at a temperature above the freezing point and is therefore nonmonotonic [35]. For example, this nonmonotonic equation of state can result in the phenomenon of cabbeling, whereby two hypopycnal parcels of water can interact to create a hyperpycnal parcel [35]. Monotonic intervals of the nonlinear equation of state

can also yield a cabbeling-like phenomenon known as *weak cabbeling*, where the mean density of the parent parcels is not equal to the density evaluated at the mean temperature of the parent parcels [36].

As discussed, the coherent structures of density driven currents modulate the transport of mass and energy and have accordingly been studied in a variety of contexts [10,12,22,27,29,37,38], but to our knowledge the modulation of coherent structures by the nonlinear equation of state for cold, fresh water is a nascent field of study. Grace *et al.* [36] simulated two-dimensional gravity currents in a free-slip domain using the equation of state for cool, fresh water. They used temperatures in a monotonic interval below the temperature of maximum density (T_{md}). In this setting hyperpycnal currents are warmer than the ambient fluid, whereas hypopycnal currents are cooler. The authors observed asymmetries in the position of the current front and shear-instability driven vertical fluxes of mass and momentum between hypo- and hyperpycnal currents with equivalent initial Gr. This is in direct contrast to the symmetry of two-dimensional, noncabbeling gravity currents demonstrated in Fig. 11 of Härtel *et al.* [17]. In a subsequent investigation, researchers selected intruding and ambient temperatures from an interval containing T_{md} and described the effect of strong cabbeling on these same phenomena [35,39]. In the present study we aim to extend this line of research by investigating modulations of the development and evolution of the lobe-cleft instability by the nonlinear, nonmonotonic equation of state for fresh water.

The remainder of this paper is organized as follows. In Sec. II, we state the governing equations and the numerical methods we use to solve them. We also define secondary variables used to investigate the stress and mixing induced by the current. In Sec. III we present the results of our simulations. First, we discuss the qualitative evolution of the gravity current by observing the effect of shear and lobe-cleft instabilities on the temperature field; we will emphasize descriptions of the structures generated by the lobe-cleft instability. We will then relate the qualitative evolution of the temperature field to quantitiative trends in the speed of the currents, the position of the currents, the bed-stresses along the contact boundaries (i.e., the bottom boundary for sinking currents and the top boundary for floating currents), and in the mixing rate of temperature. As will be shown, the evolution of the current, and the trends in the stresses and mixing induced by the current, will vary for conjugate currents. In Sec. IV we summarize our results and proposed mechanisms before describing future directions for this work.

II. METHODS AND THEORY

A. Governing equations and numerical methods

All simulations reported herein were performed using SPINS, a pseudospectral collocation solver for the stratified, incompressible Navier Stokes equations [40]. As such, the accuracy of the simulations scale with the number of grid points. To prevent aliasing, an exponential filter is used to mitigate the accumulation of energy in the small length scales.

The governing equations, under the Boussinesq approximation are as follows [41]:

$$\frac{D\vec{u}}{Dt} = -\frac{1}{\rho_0}\nabla P - g\frac{\rho'}{\rho_0}\hat{k} + \nu\nabla^2\vec{u}, \tag{1}$$

$$\nabla\cdot\vec{u} = 0, \tag{2}$$

$$\frac{DT}{Dt} = \kappa\nabla^2 T, \tag{3}$$

where the x axis points streamwise and is aligned with the flat tank bottom, the z axis points vertically and is aligned with the left wall of the tank, and the spanwise y axis is determined by the right-hand rule. Note that we use the material derivative, $\frac{D}{Dt}$, in Eqs. (1) and (3). The dimensions of the domains are $\tilde{L}_x \times \tilde{L}_y \times \tilde{L}_z = 153.6 \times 12.8 \times 30.0$ cm, and we use an $N_x \times N_y \times N_z = 1536 \times 128 \times 300$ grid. We employ free-slip boundary conditions along $x = 0, \tilde{L}_x$, and $y = 0, \tilde{L}_y$; we use no-slip conditions along $z = 0, \tilde{L}_z$ to trigger the lobe-cleft instability. We denote the ve-

TABLE I. Parameters for the equation of state [Eq. (5)].

T_{md}	C	ρ_0
(°C)	(kg °C^{-2} m^{-3})	(kg m^{-3})
3.98	7.6×10^{-6}	999.974

locity by $\vec{u} = [u(x, y, z, t), v(x, y, z, t), w(x, y, z, t)]$, the density by $\rho(x, y, z, t)$, the temperature by $T(x, y, z, t)$, and the pressure by $P(x, y, z, t)$. g is the acceleration due to gravity, ν is the kinematic viscosity, and κ is the thermal diffusivity. $\hat{k}$ is the unit vector pointing in the z direction.

We have decomposed the density as follows:

$$\rho = \rho_0 + \rho'(x, y, z, t), \tag{4}$$

where ρ' represents fluctuations around a hydrostatic background state, ρ_0. The buoyancy term associated with ρ_0 is balanced by a hydrostatic pressure term. Hence, the vertical gradient of the hydrostatic pressure and $-g\rho_0\hat{k}$ cancel each other out and do not appear in Eq. (1); instead, P represents the dynamic pressure and buoyant forcing is due solely to the fluctuation, ρ'. We use the following equation of state for the fluctuation:

$$\rho' = -C(T - T_{\mathrm{md}})^2. \tag{5}$$

This is a quadratic fit [39,42] to the freshwater, surface-pressure limit of the equation of state of McDougall *et al.* [43], and it is suitable for cold, fresh water less than approximately 10 °C [39]. Alternative equations of state include the full equation of state of McDougall *et al.* [43] or the freshwater limit of the fit to the UNESCO equation of state by Brydon *et al.* [44]. Note that the total density in Eq. (4) attains its maximum value of ρ_0 at $T_{\mathrm{md}} \approx 3.98$ °C, which is the *temperature of maximum density*. Thus, the dynamic pressure and buoyant forcing are due to deviations in T from T_{md}. The values of C, T_{md}, and ρ_0 are in Table I.

The system is initialized with the following stratification:

$$T(x, y, z) = T_a + \frac{\Delta T}{4}\left[1 + \beta\tanh\left(\frac{z - z_\ell}{\delta_z}\right)\right]\left[1 - \tanh\left(\frac{x - x_\ell}{\delta_x}\right)\right], \tag{6}$$

where $\Delta T = T_i - T_a$, $\delta_x = \delta_z = 1.00$ cm, and $x_\ell = 19.2$ cm. z_ℓ, T_i, T_a, and β are varied as part of the numerical experiments, and their values will be stated in Sec. II C. These quantities will be defined and discussed in greater detail in Sec. II B and II C; for now, it suffices to say that $\delta_x = \delta_z$ is the initial width of the interface between the intruding and ambient fluid, x_ℓ is the initial width of the intruding fluid, and z_ℓ is the height of the intruding fluid.

B. Characteristic scales and dimensionless parameters

We perform our numerical experiments by simulating the dimensional equations presented in the previous subsection, but we shall use nondimensional quantities for portions of our analysis. In

TABLE II. The parameters characterizing each experiment. As mentioned in the text, $\tilde{H} = \sqrt{\tilde{x}_\ell \tilde{z}_\ell}$ is the characteristic length, Gr is the Grashof number, $\tilde{t}_c$ is the characteristic time, and $\delta_x = \delta_z$ is the dimensionless initial width of the interface between the ambient and intruding fluid.

Case	$\tilde{H}(cm)$	Gr	$\tilde{t}_c(s)$	$\delta_x = \delta_z$
B/T-High	23.52	6.069×10^6	22.45	4.252×10^{-2}
B/T-Med	16.63	2.146×10^6	18.87	6.013×10^{-2}
B/T-Low	11.76	7.586×10^5	15.87	8.503×10^{-2}

the remainder of the text, dimensional variables will be represented with tildes (e.g., $\tilde{T}$). Standard physical constants such as g, ν, and κ are understood to be dimensional and will not have tildes.

We nondimensionalize our lengths via

$$(x, y, z) = (\tilde{x}/\tilde{H}, \tilde{y}/\tilde{H}, \tilde{z}/\tilde{H}),$$

where $\tilde{H} \equiv \sqrt{\tilde{x}_\ell \tilde{z}_\ell}$. Our decision to use this length is discussed in the final paragraph of Sec. II C. The dimensionless temperature is given by

$$T = \frac{\tilde{T} - \tilde{T}_a}{\tilde{T}_i - \tilde{T}_a},$$

This has the effect of setting the temperature of the ambient fluid to 0 and the intruding fluid to 1. Similarly, we have

$$\rho' = \frac{\tilde{\rho}' - \tilde{\rho}'(\tilde{T}_a)}{\tilde{\rho}'(\tilde{T}_i) - \tilde{\rho}'(\tilde{T}_a)},$$

where $\tilde{\rho}'$ is given by Eq. (5); this also sets the density of the ambient fluid to 0, and of the intruding fluid to 1.

The characteristic velocity and time are

$$\tilde{U}_b = \sqrt{\frac{|\Delta\tilde{\rho}|}{\tilde{\rho}_0} g\tilde{H}}, \tag{7}$$

$$\tilde{t}_c = \frac{\tilde{H}}{\tilde{U}_b}, \tag{8}$$

where $|\Delta\tilde{\rho}| = |\tilde{\rho}'(\tilde{T}_i) - \tilde{\rho}'(\tilde{T}_a)|$.

These are commonly used scales [16–18,36,39], with the exception of $\tilde{H}$, which is the geometric average of the lock-release depth and length. We use the geometric average to compare our cases, because we varied $\tilde{z}_\ell$ without varying $\tilde{x}_\ell$. We will explain this decision in Sec. II C.

Grace *et al.* [39] constructed a dimensionless parameter,

$$\Theta \equiv \frac{\tilde{T}_i - \tilde{T}_a}{\tilde{T}_{\mathrm{md}} - \tilde{T}_a}, \tag{9}$$

that allowed them to thoroughly classify the effect of the nonlinearity of the equation of state of fresh water on the behavior of two-dimensional gravity currents in free-slip domains. In our simulations, we will have cases with $\tilde{T}_{\mathrm{md}} \approx \tilde{T}_a$, so we will instead use the parameter

$$\Gamma = \frac{1}{\Theta}. \tag{10}$$

As noted by Grace *et al.* [39], this is the dimensionless temperature of maximum density. Thus, $\Gamma = 1$ corresponds to cases where $\tilde{T}_i = \tilde{T}_{\mathrm{md}}$, and $\Gamma = 0$ corresponds to cases where $\tilde{T}_a = \tilde{T}_{\mathrm{md}}$.

These scales and parameters allow us to nondimensionalize Eqs. (1)–(3) as follows [39]:

$$\frac{D\vec{u}}{Dt} = -\nabla P + \frac{(T - 2\Gamma)T}{|1 - 2\Gamma|}\hat{k} + \frac{1}{\sqrt{\mathrm{Gr}}}\nabla^2\vec{u}, \tag{11}$$

$$\nabla \cdot \vec{u} = 0, \tag{12}$$

$$\frac{DT}{Dt} = \frac{1}{\sqrt{\mathrm{GrPr}^2}}\nabla^2 T. \tag{13}$$

Note that the absolute value sign in the buoyancy term arises because the left-hand side of Eq. (1) has the characteristic scale $\tilde{U}_b^2/\tilde{H} = g|\Delta\tilde{\rho}'|/\rho_0$.

The viscosity term in Eq. (11) and diffusion term in Eq. (13) are scaled by the dimensionless quantities $1/\sqrt{\mathrm{Gr}}$ and $1/\sqrt{\mathrm{GrPr}^2}$, respectively. The Grashof number[1] is

$$\mathrm{Gr} = \left(\frac{\tilde{U}_b \tilde{H}}{\nu}\right)^2. \tag{14}$$

This characterizes the stability of the gravity current, in addition to the qualitative and quantitatve features of the gravity current and the lobe-cleft structures [10,12,15,16,18,20]. The Prandtl number is

$$\mathrm{Pr} = \frac{\nu}{\kappa}, \tag{15}$$

which characterizes the diffusion of momentum relative to the diffusion of heat in the system; in all cases $\mathrm{Pr} = 10$.

Though it does not appear in the equations of motion, we will also make use of the Froude number,

$$\mathrm{Fr} = \frac{\tilde{u}_c}{\tilde{U}_b}, \tag{16}$$

where $\tilde{u}_c$ is the speed of the gravity current. After an adjustment period, gravity currents enter the slumping phase where they travel with a constant speed [13]. After this, they can enter the inertial phase and afterwards the viscous phase [although some currents skip the inertial phase entirely if Re (the Reynolds number) or the lock-release volume are sufficiently small]; these periods are characterized by current speed, and thereby Fr, obeying a distinct power law in time [12,13,19]. The currents in the present investigation remain in the slumping phase for the majority of the simulation, so we do not report on such power laws.

C. The numerical experiments

We simulate gravity currents initialized by a partial-depth lock-release; that is, the height initial region of the intruding fluid is less than the height of the domain ($\tilde{z}_\ell < \tilde{L}_z$). The numerical experiments involve adjusting $\tilde{z}_\ell$, β, $\tilde{T}_i$, and $\tilde{T}_a$. Varying $\tilde{z}_\ell$ changes $\tilde{H}$, and thereby changes Gr, which measures how turbulent we can expect a given current to be. Since the dimensional interface width, and the lock-release length are fixed the values of δ_x, δ_z, and x_ℓ also vary across the cases. When $\beta = -1$, $\tilde{T}_i = 4.0°\mathrm{C}$, and $\tilde{T}_a = 1.5°\mathrm{C}$, the initial condition is a region of warm, dense fluid will collapse and sink into the much larger region of cool, light fluid. *These are the B-cases*, but we also refer to these as the bottom cases; here $\Gamma = 0.99$. A schematic is presented in Fig. 1. When $\beta = 1$, $\tilde{T}_i = 1.5°\mathrm{C}$, and $\tilde{T}_a = 4.0°\mathrm{C}$, the initial condition is a region of cool, light fluid shorter than $\tilde{L}_z$ that will collapse and float over a much larger region of warm, dense fluid. *These are the T-cases*, but we also refer to these as the top cases; here $\Gamma = 0.01$. We do not present a schematic for these cases; the configuration is essentially the same as Fig. 1, but the blue lock-release region is adjacent to the top boundary instead of the bottom boundary. When we discuss the interaction between bottom (top) currents and the bottom (top) boundary, we will often refer to the bottom (top) boundary as the *contact boundary*. We will use Δz when referring to distances measured from the contact boundary; accordingly, Δz is always non-negative.

Note that the nondimensional governing equations [Eqs. (11)–(13)] imply that, instead of 1.5 °C, we could use $\tilde{T}_i = 6.5\,°\mathrm{C}$ ($\tilde{T}_a = 6.5\,°\mathrm{C}$) for the B-cases (for the T-cases) and observe identical outcomes, since we would still have $\Gamma = 0.99$ ($\Gamma = 0.01$).

To summarize, we create two currents with equivalent initial $g|\Delta\tilde{\rho}|/\tilde{\rho}_0$ due to both currents having equivalent $|\tilde{T}_i - \tilde{T}_a|$; however, in one case $\tilde{T}_a \approx \tilde{T}_{\mathrm{md}}$, while in the other $\tilde{T}_i \approx \tilde{T}_{\mathrm{md}}$. *We shall*

[1]This is also the square of a Reynolds number.

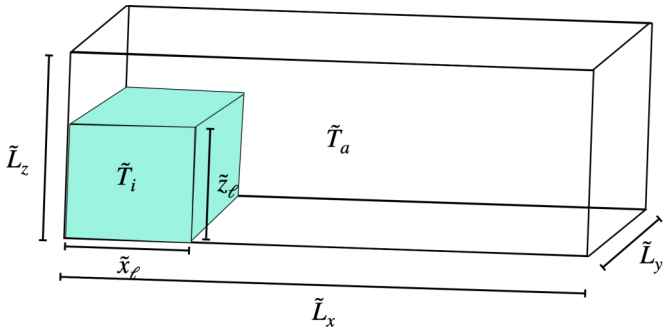

FIG. 1. A schematic of the initial experimental configuration for the bottom cases. As mentioned in the text, $\tilde{T}_i$ is the temperature of the intruding fluid, $\tilde{T}_a$ is the temperature of the ambient fluid, $\tilde{L}_x$ is the streamwise length of the domain, $\tilde{L}_y$ is the spanwise extent of the domain, $\tilde{L}_z$ is the height of the domain, $\tilde{x}_\ell$ is the length of the lock-release region, and $\tilde{z}_\ell$ is the height of the lock-release region.

henceforth refer to such pairs as "conjugate." Note that the initial states of conjugate currents are symmetric under the transformation

$$(y, z) \to (L_y - y, L_z - z).$$

In Sec. III, we demonstrate that this symmetry is broken over time.

We also increase $\tilde{z}_\ell$, as this will destabilize the systems by increasing the characteristic velocity and length scales. Our objective is therefore to observe how differences between conjugate currents manifest as the inherent stability of the system decreases. The parameters characterizing our experiments can be found in Table II.

In varying $\tilde{z}_\ell$ without varying $\tilde{x}_\ell$, $\tilde{\delta}_x$, or $\tilde{\delta}_z$, a simple experimental variation in a dimensional system produces a number of disjunct variations in parameter space. For example, changing $\tilde{z}_\ell$ while holding $\tilde{x}_\ell$ fixed affects the aspect ratio of the lock-release region; this could obfuscate the source of discrepancies between trends of cases with different Gr, as the volume and aspect ratio of the lock-release region modulate the duration (and existence) of the inertial and viscous phases of gravity currents [13]. However, our simulations end before fully entering either phase, so this will not concern us. To be more precise, the B/T-High currents reached the end of domain shortly after $t = 10$; we therefore stopped the B/T-Med and B/T-Low simulations at the same dimensionless time. As a result, none of the systems fully entered the inertial or viscous phases. The evolution of the currents will be discussed in greater detail in Sec. III.

To verify our use of $\tilde{H} = \sqrt{\tilde{x}_\ell \tilde{z}_\ell}$ as the characteristic length scale, we conducted two-dimensional simulations of conjugate currents, which we do not report on, where we did scale $\tilde{x}_\ell$, δ_x, and δ_z with $\tilde{z}_\ell$. We observed differences between conjugate currents consistent with our three-dimensional results, which we shall report on in Sec. III. Altering $\tilde{z}_\ell$, and using $\tilde{z}_\ell$ as the characteristic length instead of $\sqrt{\tilde{x}_\ell \tilde{z}_\ell}$ generated trends in the differences between the dimensionless current speed and front location of conjugate currents. These dimensionless trends are consistent with our three-dimensional results, but only if we nondimensionalize our three-dimensional cases using $\sqrt{\tilde{x}_\ell \tilde{z}_\ell}$ as the characteristic length scale.

D. Stress along the contact boundaries

We use no-slip boundary conditions along the top and bottom of the domain, so the gravity currents will generate stress along these surfaces. The stress in the x_i direction ($i = 1, 2$; $x_1 = x$, $x_2 = y$) along the top of the domain is given by

$$\tilde{\tau}_{x_i} = -\tilde{\rho}_0 \nu \left. \frac{\partial \tilde{u}_i}{\partial \tilde{z}} \right|_{\tilde{z}=\tilde{L}_z}, \tag{17}$$

and along the bottom by

$$\tilde{\tau}_{x_i} = \tilde{\rho}_0 \nu \frac{\partial \tilde{u}_i}{\partial \tilde{z}}\bigg|_{\tilde{z}=0}. \tag{18}$$

We do not have a similar stress for $i = 3$ (the z direction) because our fluid is incompressible, and we assume no-slip boundary conditions. In our results, we present the nondimensionalized boundary stresses, which are scaled by $\tilde{\rho}_0 \tilde{U}_b^2$.

E. Mixing

In a fixed domain D with a (dimensional) volume V, the domain-averaged temperature is

$$\langle \tilde{T} \rangle = \frac{1}{V} \int_D \tilde{T} dV. \tag{19}$$

We can then define the variance as

$$\mathrm{Var}(\tilde{T}) = \frac{1}{V} \int_D (\tilde{T} - \langle \tilde{T} \rangle)^2 dV. \tag{20}$$

This immediately reduces to

$$\mathrm{Var}(\tilde{T}) = \langle \tilde{T}^2 \rangle - \langle \tilde{T} \rangle^2. \tag{21}$$

The time derivative of the above is then

$$\frac{d}{d\tilde{t}} \mathrm{Var}(\tilde{T}) = \frac{d}{d\tilde{t}} \langle \tilde{T}^2 \rangle - 2 \langle \tilde{T} \rangle \frac{d}{d\tilde{t}} \langle \tilde{T} \rangle. \tag{22}$$

If we assume that D is fixed, and that the boundary of D obeys the no-flux and no-pass conditions, then

$$\frac{d}{d\tilde{t}} \mathrm{Var}(\tilde{T}) = -\frac{1}{V} \int_D 2\kappa \tilde{\partial}_j \tilde{T} \tilde{\partial}_j \tilde{T} dV. \tag{23}$$

Note that $\tilde{\partial}_j = \partial / \partial \tilde{x}_j$, and we are using the Einstein summation convention for compactness. The decrease in the global variance of temperature is therefore driven solely by the domain integral of the quantity

$$\tilde{\chi}_T = 2\kappa \partial_j \tilde{T} \partial_j \tilde{T}. \tag{24}$$

As a shorthand, define

$$\tilde{\chi}_T^D = \frac{1}{V} \int_D 2\kappa \partial_j \tilde{T} \partial_j \tilde{T} dV. \tag{25}$$

We will call $\tilde{\chi}_T$ the local mixing rate and $\tilde{\chi}_T^D$ the global mixing rate. The local mixing rate is to $\mathrm{Var}(\tilde{T})$ what viscous dissipation is to kinetic energy, so it is also known as the dissipation of temperature variation [45]. Finally, we shall denote the horizontal average of the local mixing rate by $\tilde{\chi}_T^H$. That is,

$$\tilde{\chi}_T^H(\tilde{z}, \tilde{t}) \equiv \frac{1}{\tilde{L}_x \tilde{L}_y} \int_0^{\tilde{L}_y} \int_0^{\tilde{L}_x} \tilde{\chi}_T d\tilde{x} d\tilde{y}. \tag{26}$$

The quantities defined by Eqs. (24)–(26) are scaled by $(\tilde{T}_i - \tilde{T}_a)^2 / \tilde{t}_c$, and the nondimensional local mixing rate is

$$\chi_T = \frac{2}{\sqrt{\mathrm{GrPr}^2}} \partial_j T \partial_j T, \tag{27}$$

where ∂_j is now shorthand for $\partial / \partial x_j$.

F. Baroclinic vorticity

If we nondimensionalize and then take the curl of Eq. (1), then we get the vorticity equations:

$$\frac{D\omega_x}{Dt} = (\vec{\omega}\cdot\nabla)u + 2\frac{(T-\Gamma)}{|1-2\Gamma|}\frac{\partial T}{\partial y} + \frac{1}{\sqrt{\mathrm{Gr}}}\nabla^2\omega_x, \tag{28}$$

$$\frac{D\omega_y}{Dt} = (\vec{\omega}\cdot\nabla)v - 2\frac{(T-\Gamma)}{|1-2\Gamma|}\frac{\partial T}{\partial x} + \frac{1}{\sqrt{\mathrm{Gr}}}\nabla^2\omega_y, \tag{29}$$

$$\frac{D\omega_z}{Dt} = (\vec{\omega}\cdot\nabla)w + \frac{1}{\sqrt{\mathrm{Gr}}}\nabla^2\omega_z. \tag{30}$$

The first term on the right-hand side of each equation is the vortex tilting and stretching term, and the last term on the right-hand side of each equation accounts for viscous forcing [41]. The middle term of the right-hand side of Eqs. (28) and (29) describe the quantity known as *baroclinic vorticty generation* [41]; they account for the effects of the buoyant force on vorticity:

$$\frac{\partial\omega_{\mathrm{clin},x}}{\partial t} = 2\frac{(T-\Gamma)}{|1-2\Gamma|}\frac{\partial T}{\partial y}, \tag{31}$$

$$\frac{\partial\omega_{\mathrm{clin},y}}{\partial t} = -2\frac{(T-\Gamma)}{|1-2\Gamma|}\frac{\partial T}{\partial x}, \tag{32}$$

where $\omega_{\mathrm{clin},x}$ and $\omega_{\mathrm{clin},y}$ are respectively the x component and y component of the rate of baroclinic vorticity generation. The initial streamwise temperature gradient generates $\omega_{\mathrm{clin},y}$, which initiates the motion of the gravity current. When the gravity current begins to form lobe-cleft structures, a spanwise temperature gradient forms and generates $\omega_{\mathrm{clin},x}$. The streamwise baroclinic vorticity, in turn, induces motion in the vertical and spanwise directions. Increasing the x and y components of the vorticity allow for the production of horseshoe/hairpin vortices [46], the interactions of which are believed to govern the merging and splitting processes in gravity currents [16].

III. RESULTS

Before we present our results, we wish to discuss the common format of the three- and six-panel figures. In each of these figures, the top row of panels corresponds to the B/T-High cases, the middle row to the B/T-Med cases, and the bottom row to the B/T-Low cases. In the six-panel figures, the left column corresponds to the bottom cases, and the right column corresponds to the top cases. When we use Δz, we are referring to the distance from the *contact boundary*—i.e., the boundary over/under which the bottom/top current flows—and not the vertical height. As such, the right column panels are effectively "flipped" upside-down. For example, in Fig. 2, the currents in Figs. 2(b), 2(d) and 2(f) are traveling under the top boundary.

A. Qualitative description of current evolution

Initially rectangular intrusions collapse towards the boundary and take the form of a round head with a trailing rectangular tail [1]. The currents accelerate and then enter the slumping phase during which they move with a constant velocity. Shortly after entering the slumping phase, two instabilities develop: first, shear instabilities along the top and back of the current head, and second, lobe-cleft instabilities along the front and bottom of the current head. The former manifest as billows oriented parallel to the spanwise axis (see Fig. 2), and the latter manifest as rows of bulges along the front of the current. The currents evolve consistently with past work [1,2,10,12,15–17,19,20,24], but—as we will show—the specifics of the evolution of the two- and three-dimensional structures of the current differ for $\Gamma \approx 1$ (B-cases) and $\Gamma \approx 0$ (T-cases).

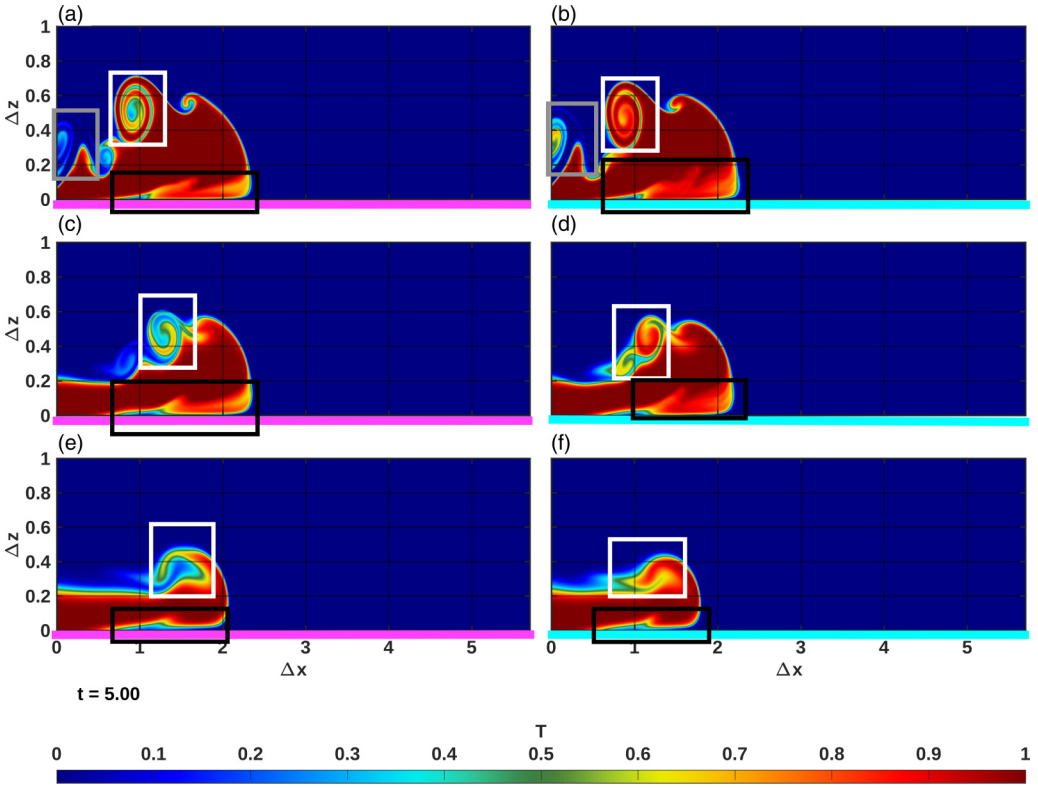

FIG. 2. Spanwise mean of T at time $t = 5$. The left panels correspond to B-cases, and the right panels correspond to T-cases. For clarity, the contact boundary is coloured pink when it corresponds to the bottom boundary, and it is coloured cyan when it corresponds to the top boundary. The panels in the top row correspond to the B/T-High cases ($\mathrm{Gr} = 6.069 \times 10^6$), the middle row to the B/T-Med cases ($\mathrm{Gr} = 2.146 \times 10^6$), and the bottom row to the B/T-Low cases ($\mathrm{Gr} = 7.586 \times 10^5$). The horizontal axis measures the width/spanwise extent of the domain. This is a frame from the supplementary video HOR-T-PROF. The vertical axis measures the distance from the contact boundary instead of the vertical coordinate (i.e., the currents in the right panels are "upside-down" and are actually floating under the top boundary). This is a frame from the supplementary video VER-T-PROF. The gray rectangles highlight the dipoles from the B/T-High cases. The white rectangles surround billows produced by the shear instability. The black rectangles surround structures produced by the lobe-cleft instability; these will be discussed in Sec. III A 2.

1. The shear instability

We begin by discussing the shear instability. In Figs. 2 and 3 we plot the spanwise averaged temperature for each case at time $t = 5$ and $t = 10$, respectively. We observe that the proportion of fluid within the head versus the tail depends on Gr. In the bottom panels of Fig. 2 and 3, the tails of currents from the B/T-Low cases contain the majority of the fluid, while the heads are tall, thin structures that slowly decay over the duration of the simulation. In contrast, in the B/T-High cases the intruding fluid is contained almost entirely within the head of the current. Fittingly, the currents from the B/T-Med cases have both rounded heads, and stable, wide tails. In the B/T-High cases the volume-dominant head leaves behind a long, thin tail which goes unstable and forms a dipole; the dipole from each case is highlighted by a gray rectangle in Figs. 2(a) and 2(b) and Figs. 3(a) and 3(b). The dipole is eventually ejected from the tail, and the dipole from the B-High case is ejected farther from the contact boundary than the T-High dipole; this is consistent with the results from Grace *et al.* [36].

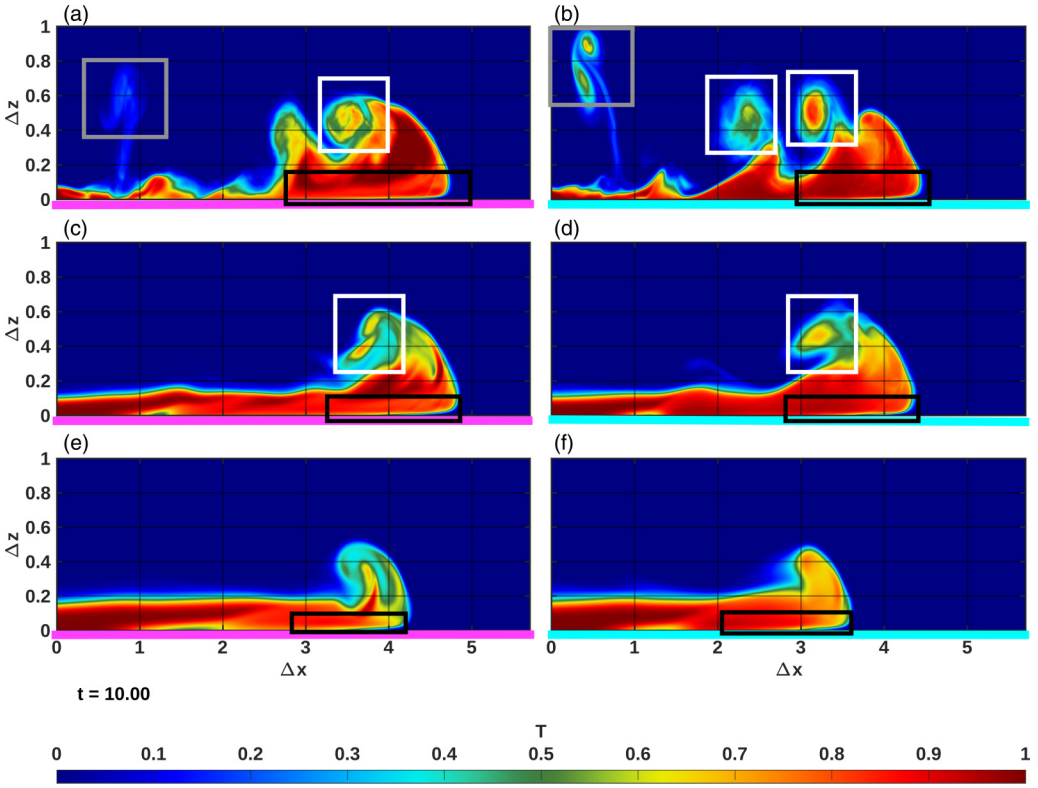

FIG. 3. Same as Fig. 2 but at $t = 10.0$. The gray rectangles highlight the dipoles from the B/T-High cases. The white rectangles surround billows.

The shear along the collapsing currents generates billows along the tops and backs of the current heads, as is often observed [1,2,12]. We highlight the billows with white rectangles in Fig. 2. The billows of the B/T-High and B/T-Med cases consist of coiled filaments. The filaments from bottom currents are thinner than those from the top currents. Furthermore, the filaments of the top currents are coiled tighter, so their billows entrain less ambient fluid than those of equivalent bottom currents. In Fig. 3 it appears that the billows are no longer well defined and have effectively been destroyed; this, however, is a misleading artifact of averaging the field in the spanwise direction.

In Fig. 4 we present the three-dimensional T fields from the B/T-High cases at time $t = 10$. We use an opacity map that sets regions with $T < 0.05$ and $T > 0.95$ to be transparent. Figure 4(a) corresponds to the B-High case and Fig. 4(b) to the T-High case. In this figure, we see that the billows are still attached to the current head and have a highly three-dimensional structure: namely the billows have spanwise undulations. The undulations are produced by folds in each billow, which are highlighted in Fig. 4. The folds have the effect of segmenting the billow, with the size of the segments being similar to the size of the lobes at the front of the current (which are also highlighted via annotations). These lobes are produced by the mature lobe-cleft instability, which we will discuss in detail in Sec. III A 2; for now, it suffices to note that by "mature," we mean that the lobe-cleft instability has developed secondary instabilities. The correlation between the size of segments and lobes suggests that the billows are three-dimensionalized by the lobe-cleft instability. Notice that the segments in Fig. 4(b) have a greater vertical offset than the segments in Fig. 4(a). Indeed, this vertical offset is why the billows in the spanwise average of the T field in Fig. 3(b) appear to be ejected from the current head, whereas the billows in Fig. 3(a) appear to be attached. To summarize, the pale blue regions in Fig. 3 indicate regions where the billows possess a large degree of spanwise

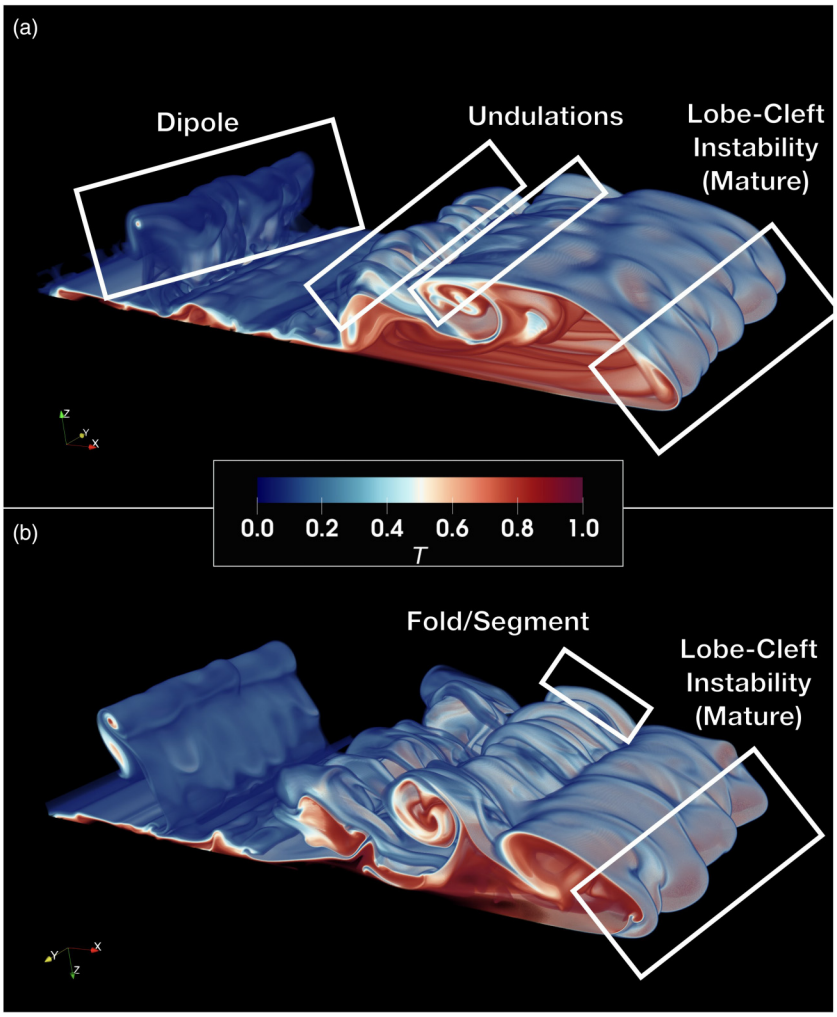

FIG. 4. The interface between the intruding and ambient fluid for the B/T-High cases at time $t = 10$. Regions where $T < 0.5$ or $T > 0.95$ have been made transparent. Panel (a) is from the B-High case, and panel (b) is from the T-High case. As in Fig. 2 and 3, the T-High system has been rotated π radians about the x axis so that it is easier to compare the conjugate currents.

variation, and top current billows have more spanwise variation than the conjugate bottom current billows. The physical significance of this will be discussed in Sec. III B 3.

To reiterate, the observed asymmetric behavior is in contrast to that of noncabbeling currents, where we would expect to see little to no discrepancy in the spanwise structure of conjugate currents. For an example, refer to Fig. 2 from Härtel *et al.* [17]. There we see that the three-dimensional no-slip top and bottom currents evolve similarly until $t = 5$ and then with some slight deviations at later times due to the stochastic nature of the wake formed by the shear instability. At $t = 10$, the top and bottom current heads have a nearly identical position, shape, and volume, which is clearly not the case in our Fig. 4; this greater discrepancy must be due to weak cabbeling.

2. The lobe-cleft instability

We shall now discuss the lobe-cleft instability. In Figs. 5 and 6 we present the interface between the current head and the ambient fluid from the high-Gr cases. In both figures, the bottom row of

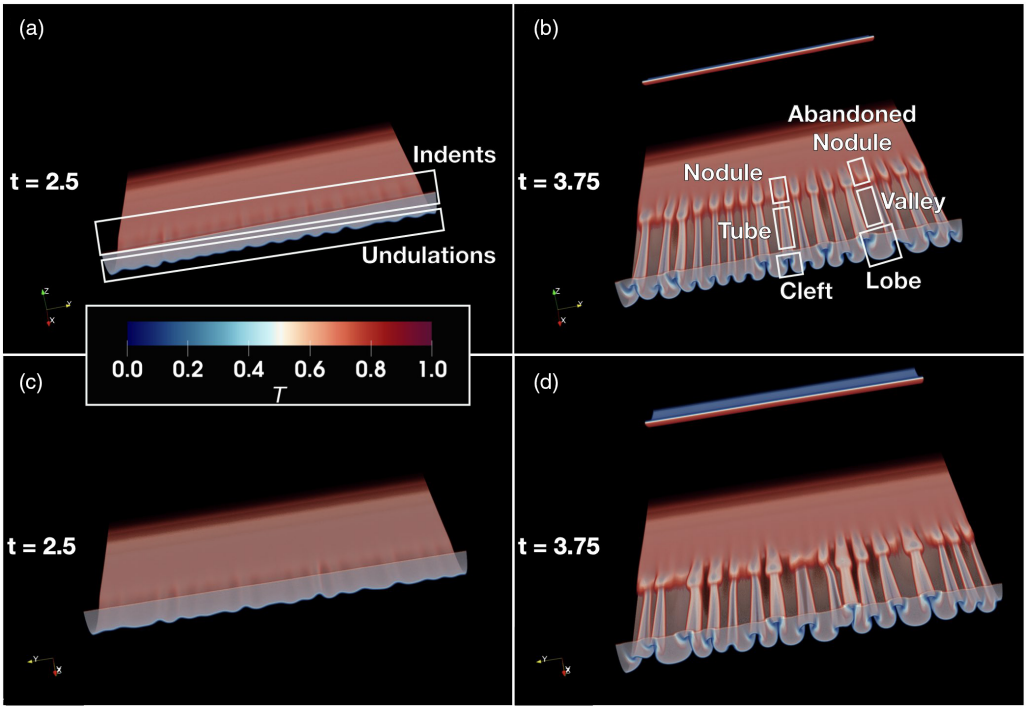

FIG. 5. The interface between the intruding and ambient fluid for the B/T-High cases at time $t = 10$. Regions where $T < 0.5$ or $T > 0.95$ have been made transparent. Panels (a) and (b) correspond to the B-High case and panels (c) and (d) to the T-High case. $\mathrm{Gr} = 6.069 \times 10^6$ in both cases. As in Fig. 2 and 3, the T-High system has been rotated π radians about the x axis so that it is easier to compare the conjugate currents. These figures focus on a window $0.2\tilde{H}$ away from the contact boundary and $2.2\tilde{H}$ behind the front of the current. The dimensionless time is stated in each panel. Annotations highlight structures produced by the lobe-cleft instability.

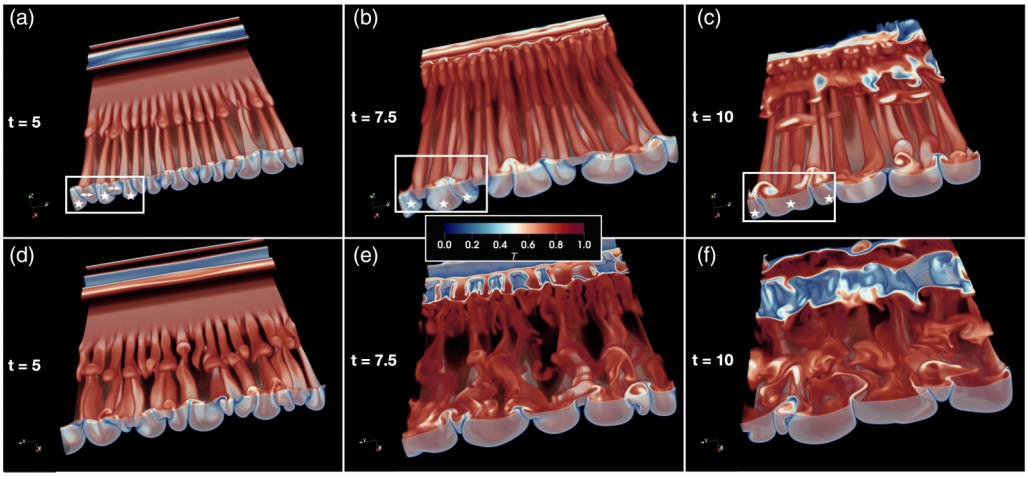

FIG. 6. Similar to Fig. 5. Panels (a)–(c) correspond to the B-High case, and panels (d)–(f) correspond to the T-High case. $\mathrm{Gr} = 6.069 \times 10^6$ in both cases. In panels (a)–(c) we use annotations to call attention to five lobes undergoing the merging process. The lobes labeled with double-headed arrows are annihilated by the adjacent lobes labeled with stars. Other lobes in panels (a)–(c) and panels (d)–(f) undergo the merging process, but we do not highlight them.

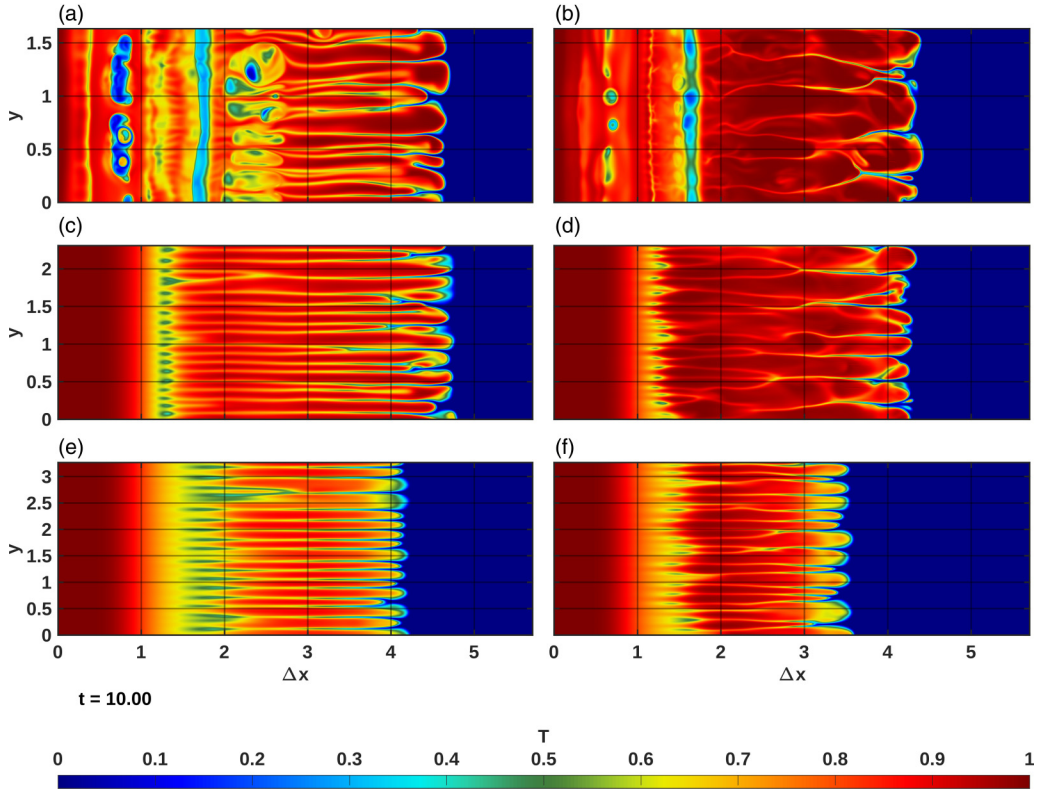

FIG. 7. $x - y$ cross section of T taken $\Delta z = 0.02$ from the contact boundary at time $t = 10$. The left panels correspond to B-cases and the right panels correspond to T-cases. The panels in the top row correspond to the -High cases (Gr $= 6.069 \times 10^6$), the middle row to the -Med cases (Gr $= 2.146 \times 10^6$), and the bottom row to the -Low cases (Gr $= 7.586 \times 10^5$). The vertical axis measures the width/spanwise extent of the domain. This is a frame from the supplementary video HOR-T-PROF.

panels correspond to the T-High case and the top row to the B-High case. We restrict our focus to the lobe-cleft structures and truncate the interface to only include a region $\Delta x = 2.2$ behind the wave front and $\Delta z = 0.2$ away from the contact boundary; there is no truncation in the spanwise direction.

Figures 5(a) and 5(c) correspond to the early lobe-cleft instability. The early stages of the instability result in spanwise undulations at front of the current; these undulations leave elongated indents in the lower interface. We use annotations in Fig. 5(a) to call attention to these features. In Figs. 5(b) and 5(d), we depict secondary instabilities with annotations that highlight the resultant structures. In Fig. 5(b) and 5(d), we see that the undulations from 5(a) and 5(c) (respectively) have evolved into the iconic lobes and clefts described in previous investigations [2,3,10,15–17,19,20]. Just as the undulations were trailed by indentations, the lobes are now trailed by valleys, and the clefts are trailed by tubes (which are themselves trailed by structures we henceforth refer to as *nodules*). Note that some nodules do not correspond to a tube and are therefore "abandoned." In spite of the secondary instabilities in Figs. 5(b) and 5(d), the tubes are still "orderly." By orderly, we mean that the tubes and valleys are parallel and oriented along the streamwise direction. To our knowledge, these nodules, tubes, and valleys are not often discussed in the lobe-cleft literature, though they appear to correspond to the horseshoe vortices in Fig. 7 from Dai and Huang [16] and to the streaks in Fig. 8(f) from Didden and Maxworthy [47]. Dai and Huang [16] also allude to the

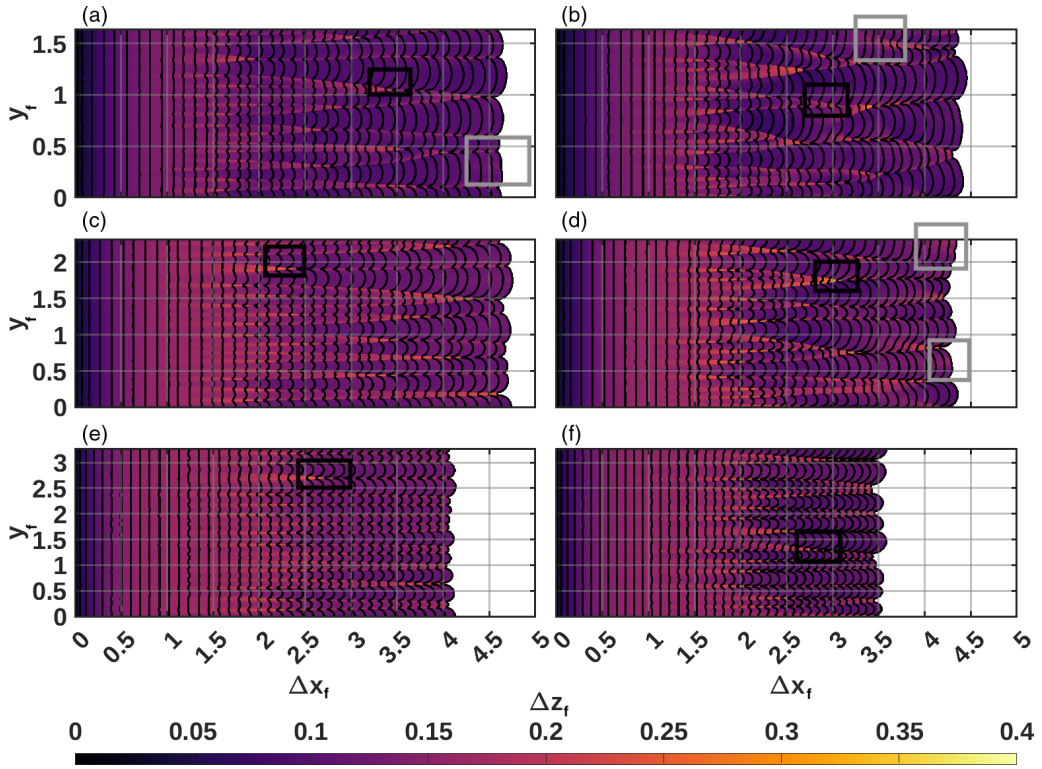

FIG. 8. The height of the current front. Here Δz is the distance from the contact boundary to the front and Δx is the horizontal displacement of the front (i.e., the distance traveled by the front from the lock-release region). The superimposed black curves denote the horizontal displacement of the front every $t = 0.25$. The left column of panels are from the bottom cases, and the right column are from the top cases. The panels in the top row correspond to the B/T-High cases ($\mathrm{Gr} = 6.069 \times 10^6$), the middle row to the B/T-Med cases ($\mathrm{Gr} = 2.146 \times 10^6$), and the bottom row to the B/T-Low cases ($\mathrm{Gr} = 7.586 \times 10^5$). Black rectangles highlight a subset of the merging events, and gray rectangles highlight a subset of the splitting events.

existence of these structures in the discussion of their Fig. 2, which shows an x-z cross section of the inside of the current head.

In Fig. 6 structures from the secondary instability continue to grow. At time $t = 5$, the tubes of the B-High current develop kinks [see Fig. 6(a)], and the nodules elongate. Similar effects are present in the T-High current [see Fig. 6(d)], but the kinks in the tubes are much larger, and the elongated nodules begin to deviate from the streamwise direction. That is, they are becoming disordered. This trend continues in Figs. 6(b) and 6(e) (time $t = 7.5$). In Fig. 6(b), the tubes and nodules of the B-High current are still orderly, which is in clear contrast to the behavior of the T-High case in Fig. 6(e). The nodules of the T-High current are no longer visible, and the field around the tubes has a complex, chaotic structure. Finally, in Figs. 6(c) and 6(f) ($t = 10$), the tubes of the B-High current are still orderly, whereas the tubes of the T-High current are almost entirely obfuscated by the aforementioned chaotic structures in the T field; this suggests that the inside of the T-High current is transitioning into a turbulent flow by the end of the simulation.

Notice that the lobes at the front of both currents swell and decrease in number as the current evolves. This is due to the merging process [10,16]. We use annotations in Figs. 6(a), 6(b) and 6(c) to call attention to an example. The rectangle in Fig. 6(a) contains five lobes: three labeled with stars and two labeled with double-headed arrows. In Fig. 6(b), we see that only the three lobes with stars remain. Between the events depicted in Figs. 6(a) and 6(b), half of each double-arrow lobe

was rolled into a starred neighbor. Recall that in Fig. 5(b) and 5(d), each lobe is trailed by a valley, and each cleft is trailed by a tube. This one-to-one correspondence is clearly broken in Figs. 6(c). The second lobe (counting from the left), has two tubes and one valley trailing directly behind it, whereas the first lobe and third lobes are trailed only by one tube and one valley. The second lobe, which is the largest, has also developed a small indent (visible just beneath the star), which indicates that it is about to split. This suggests that multiple tubes trailing a lobe is an unstable configuration and will initiate the well-documented splitting process [10,16].

We have discussed the lobe-cleft instability of the B/T-High cases at great length, but what of the other cases? In Fig. 7 we plot x-y cross sections of the T field taken at $\Delta z = 0.02$ for each case at $t = 10$. This is a frame from the supplemental video HOR-T-PROF [48], which we encourage the reader to view for additional insight into the internal dynamics of the current. The red regions correspond to the valleys that trail the lobes. From the cross-sections plotted in panels Figs. 7(d)–7(f) we see that the trends from the B/T-High cases also hold for the B/T-Med and B/T-Low cases. Namely, the valleys (and therefore the tubes) in the T-cases become more curved and distended than those from the B-cases as the current evolves. At every Gr, the T-case valleys are visibly wider than those of the conjugate B-case.

The lobe-cleft structures are also visible in Figs. 2 and 3; the nodules and tubes create the yellow regions highlighted by the black, rectangular annotations. At time $t = 5$ (Fig. 2; inside the black rectangles), a lump of ambient fluid is trapped under the current head. The tubes correspond to the yellow-orange region between the trapped lump and the front of the current. The tubes of the T-cases extend farther into the current head than the tubes of the B-cases. Notice that the height of the tube also increases with Gr. These trends hold for the nodules, which correspond to the yellow-orange regions protruding obliquely from the trapped lump. By $t = 10$ (Fig. 2; inside the black rectangles), the nodules and tubes cannot be distinguished in the spanwise-averaged temperature field; they are instead replaced by diffuse yellow regions emanating from the contact boundary. As with the height of the tubes, these regions are taller in the T-cases. Observe that the lumps of trapped ambient fluid have also nearly disappeared and are almost entirely incorporated into the current. This indicates that the fluid from these trapped lumps fills the inside of the nodules.

B. Quantitative analysis of current evolution

1. The position of the front, the size of the lobes, and their relation to the merging process

Investigations into the lobe-cleft instability naturally focus on the front of the current, where the instability first manifests [10,12,16,17,19–21,36]. We define the coordinates of the front at time t, $(x_f(t), y_f(t))$, as the leading points of the projection of the contour $\rho = 0.05$ onto the contact boundary. In effect, our front is the leading edge of a "digital shadowgraph." We then evaluate ρ at each $(x_f(t), y_f(t))$, and the Δz_f at which ρ takes its maximum value is taken to be the vertical distance between the front and the contact boundary at a given $(x_f(t), y_f(t))$. In Fig. 8, we use a black contour to indicate the location of the front every $t = 0.25$ from $t = 0.25$ to $t = 10.0$. These are superimposed on the $\Delta z_f(x_f(t), y_f(t))$ field between $t = 0.0$ to $t = 10.0$. Note that on the horizontal axis we measure $\Delta x_f(t) = x_f(t) - x_\ell$, which is the displacement from the initial location of the front. The contours in Fig. 8 produce plots similar to Fig. 8 from Simpson [10], to Fig. 10(a) from Cantero *et al.* [19], and to Fig. 4 from Dai and Huang [16].

In each panel of Fig. 8, the leftmost contours are straight, vertical lines. Towards the middle of the panel, however, the contours develop small bumps: These are the result of the lobe-cleft instability, and each bump corresponds to a lobe. As we move our focus rightwards, we see that the bumps in the contours become wider and less numerous. This is due to the fact that as the lobe-cleft instability matures, lobes exhibit lateral growth or decay. A trio of lobes can fuse into a pair if the two outermost lobes become larger than and absorb the intermediate lobe during a period of lateral growth [10,16]. We indicate examples of merging events using black rectangles in Fig. 8. Note that wherever we see merging, we see that Δz_f has a local maximum. Thus, when a lobe is absorbed by two neighboring lobes in the merging process, its vertical distance from the contact boundary

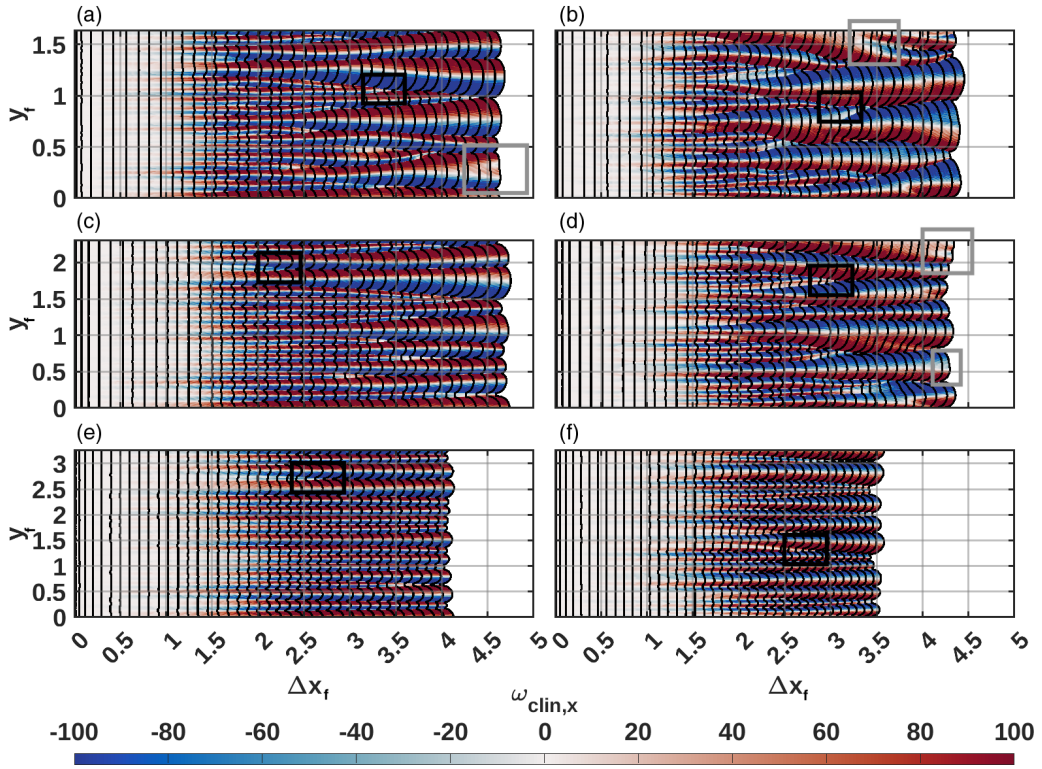

FIG. 9. Similar to Fig. 8 but plotting the x component of the baroclinic vorticity along the front instead of the vertical displacement of the front. The black and gray squares correspond, respectively, to the same merging and splitting events highlighted in Fig. 8.

increases as its lateral extent decreases. In other words, the consumed lobe is "rolled" up between its growing neighbors. We also see evidence of splitting: the process where one lobe becomes two; refer to the gray rectangles in Fig. 8 for examples.

Reference [16] argues that the merging and splitting processes are governed by vortex interactions. We present evidence for this in Fig. 9, where we plot the x component of the baroclinic vorticity (as defined in Sec. II F) sampled along the front of the current. By sampling, we mean that we evaluate the baroclinic vorticity at each $(x_f, y_f, \Delta z_f)$. Each lobe is subdivided into a red, white, or blue region, which correspond, respectively, to streamwise, null, or antistreamwise baroclinic vorticity. Thus, each lobe corresponds to the front of one horseshoe vortex, as defined by Adrian [46]. Recall that in Figs. 5(b) and 5(d), each lobe is initially bordered by two tubes.[2] Thus, the arms of the horseshoe vortices are aligned with the tubes. Indeed, the tubes are an additional source of baroclinic vortex generation, since they generate spanwise gradients in T. Take care to note that each tube is situated between two lobes, so the arms of adjacent horseshoe vortices share one tube.

In Fig. 9, the flow is oriented away from the contact boundary where a red region meets a blue region (i.e., between two lobes, within a cleft, and along a tube); similarly, the flow is oriented towards the contact boundary where a red or blue region meets a white region (i.e., in the center of a lobe and along a valley). Thus, when two lobes overtake their common neighbor, the flow along the lobe boundaries pushes the lobe upwards and onto the neighboring lobes, and thereby generates

[2]With the exception of the lobes at the $y = 0, Lz$ walls, which can only be bordered by one tube.

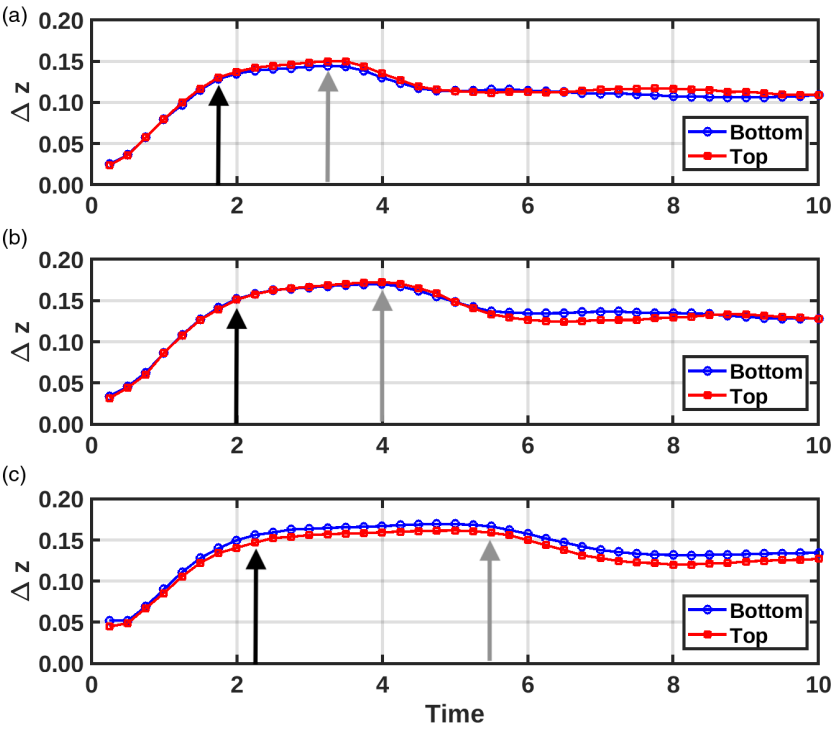

FIG. 10. The vertical distance of the nose from the contact boundary. The current velocity is the time derivative of x_N. Panel (a) corresponds to the B/T-High currents, (b) to the B/T-Med currents, and (c) to the B/T-Low currents. Δz_f is the vertical distance from the contact boundary. Black arrows indicate the emergence of the lobe-cleft instability and gray arrows indicate the time when the swelling lobes begin to interact.

the local maxima in Δz_f that correlate with merging regions in Fig. 8. The vortices of the larger lobes induce faster flows than the vortex of the intermediate lobe; the merging process ultimately results in the decoherence of the smaller vortex of the intermediate lobe. However, the arms of the smaller horseshoe vortex are still coherent along the tube. As discussed in Sec. III A 2, the lobes that remain after merging are now trailed the tubes they shared with the rolled-up lobe. That is, the arms of the annihilated vortex continue to interact with the arms of the remaining vortices in the tubes, and this interaction takes place immediately behind some of the remaining lobes. These interactions then initiate the splitting process, as is evidenced by the newly formed cleft in the second starred lobe in Fig. 6(c). The region highlighted by the gray box of Fig. 9(a) corresponds to this cleft. This previously white region is now developing a red-blue patch, which is due to the new cleft generating spanwise gradients in T. Other splitting events are also highlighted with gray rectangles.

Let x_N and Δz_N be the the spanwise mean of x_f and Δz_f, respectively. That is,

$$x_N(t) = \int_0^{y_f(t)} x_f(s)ds, \tag{33}$$

$$\Delta z_N(t) = \int_0^{y_f(t)} \Delta z_f(x_f(s), s)ds. \tag{34}$$

These are the coordinates of the nose of the gravity current, which is the front-most protrusion of the spanwise-averaged profile of the current. We plot Δz_N in Fig. 10. In every case the vertical displacement of the nose appears to increase, plateau, and then decrease towards another plateau. The first plateau correlates with the emergence and initial growth of lobe-cleft structures, and the

period of descent correlates with the maturation of the lobes and clefts; these events are labeled with arrows in Fig. 10. The lobes begin to merge half-way through the descent and continue to do so during the second plateau; the vertical displacement of the nose does not appear to change during subsequent merging events. Furthermore, the duration of the ascent of the nose does not differ between conjugate currents. The duration of the descent does, however, appear to decrease as Gr increases. The onset time of the lobe-cleft instability is clearly unaffected by whether $\Gamma = 1$ or 0 and is entirely dependent on Gr.

Consider the trapped lumps of ambient (blue) fluid inside the black, rectangular annotations of Fig. 2. These lumps are traced out by the ascent and descent of the nose; this is especially clear in the supplemental video VER-T-PROF [48]. The tubes and nodules emanating from the trapped lump are also consistent with the initiation of secondary instabilities during the descent of the nose. This is at odds with the results of Härtel *et al.* [17]. These authors argued that the volume of fluid beneath the current head is too small to generate a buoyant instability and instead state that the lobe-cleft structures are due to a unique instability that initiates near the stagnation point (just below the nose). However, following our discussion here and in Sec. III A 2, we see that the lobe-cleft instability initiates during the ascent and descent of the nose and that the instability continues to grow between the trapped fluid and the nose throughout the simulation. That is, the lobe-cleft instability is not confined to regions near the nose,[3] but it grows along the entire bottom of the current head. Furthermore, the growth of the nodules (which are generated by secondary instabilities) is driven by the trapped ambient fluid pushing into the current. Altogether, this suggests that some sort of buoyant forcing drives the lobe-cleft instability.

The dimensionless speed of a given current is $u_c = \frac{d}{dt}x_N(t)$, which is equal to Fr (as mentioned in Sec. II B). We plot this in Fig. 11. In each case the currents accelerate until they enter the slumping phase. Although the signal is noisy during the acceleration phase, the signals of conjugate currents appear to fluctuate around similar curves. Towards the end of the medium and low-Gr simulations [Figs. 11(b) and 11(c)], we see that the currents begin to decelerate; however, the simulations ended before any current fully transitioned into the inertial phase. Consistent with the results of Ref. [36], the bottom currents have greater speeds than their conjugates. Furthermore, the discrepancy between conjugate currents slowly increases in time. However, the size of the discrepancy at any moment of the slumping phase appears to decrease as Gr increases. Viscous forces also decrease as Gr increases, so this suggests that fluid friction along the current interface is stronger for top currents, and this discrepancy will disappear as $\mathrm{Gr} \to \infty$.

We note that the lobe-cleft instability does not contribute to the discrepancy in Fr, nor does it contribute to the decrease in the discrepancy with the increase of Gr. In Fig. 11, we once again use black and gray arrows to indicate the start of the lobe-cleft instability and the start of lobe swelling, respectively. The primary lobe-cleft instability always starts during the acceleration phase, so it cannot be the source of the discrepancy in Fr. Furthermore, the swelling process can start: (i) before deviations in Fr are observable [Fig. 11(a)], (ii) as the deviations begin to emerge [Fig. 11(b)], and (iii) well after the discrepancy has emerged [Fig. 11(c)]. That is, the lobe-cleft instability appears to be entirely uncorrelated with the discrepancies in Fr of conjugate currents.

Let

$$\bar{T}_y(x, z, t) \equiv \langle T(x, y, z, t)\rangle_y \equiv \frac{1}{L_y}\int_0^{L_y} T(x, y, z, t)dy, \tag{35}$$

where $\langle\rangle_y$ denotes the spanwise average. The variance of the T field in the spanwise direction is then given by $\langle(T - \bar{T}_y)^2\rangle_y$. If we then take the average of this in the x and z directions, then we get the

[3]Or, near the top of the current head, as argued in Härtel *et al.* [15].

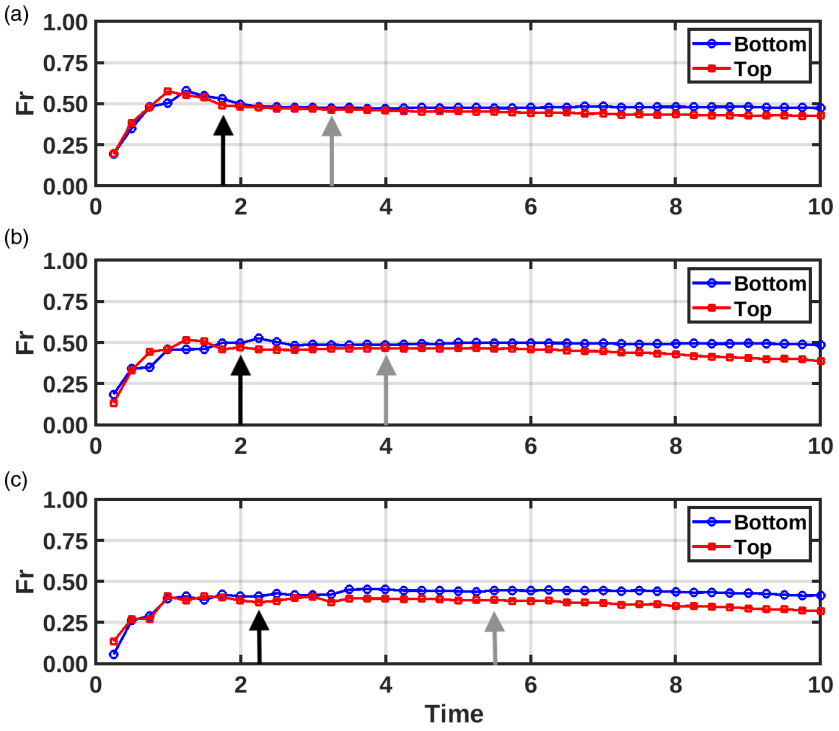

FIG. 11. Plots of Fr, as defined in Sec. II B. The current velocity is the time derivative of x_N. Panel (a) corresponds to the B/T-High cases (Gr $= 6.069 \times 10^6$), panel (b) to the B/T-Med cases (Gr $= 2.146 \times 10^6$), and panel (c) to the B/T-Low cases (Gr $= 7.586 \times 10^5$). Black arrows indicate the emergence of the lobe-cleft instability and gray arrows indicate the time when the swelling lobes begin to interact.

time-dependent scalar

$$\mathrm{Var}_y(T) \equiv \frac{1}{L_x L_z} \int_0^{L_z} \int_0^{L_x} \langle (T - \bar{T}_y)^2 \rangle_y dx dz, \tag{36}$$

which measures the three-dimensionalization of the field T at a given time.

In Fig. 12 we plot $\Delta\mathrm{Var}_y(T)$, which is $\mathrm{Var}_y(T)$ of a B-case subtract $\mathrm{Var}_y(T)$ of its conjugate T-case; that is, $\Delta\mathrm{Var}_y(T) > 0$ indicates the B-case system is more three dimensional, and $\Delta\mathrm{Var}_y(T) < 0$ indicates the T-case system is more three dimensional. The black arrows in Fig. 12 indicate the start of the lobe-cleft instability, which is when the systems begin to exhibit three-dimensional structure. We see that $\Delta\mathrm{Var}_y(T) = 0$ even after the instability initiates, which implies that the early average growth of the lobe-cleft instability is similar—if not identical—for conjugate currents. In other words, the differences between the lobe-cleft instability of conjugate currents only manifest once the instability is finite amplitude. The gray arrows in Fig. 12 correspond to the swelling of the nodes, which initiates just as $\Delta\mathrm{Var}_y(T)$ becomes negative for all Gr. Thus, the lobe-cleft instability of the top currents eventually induces more three-dimensional structure than that of their conjugate bottom currents. This, however, does not remain true for all cases. In the B/T-Low cases [Fig. 12(c)], the signal achieves a local minimum around $t = 6.75$ and then increases in value for the remainder of the simulation, with $\Delta\mathrm{Var}_y(T) > 0$ after $t = 7.5$. This indicates that the B-Low current ultimately develops more three-dimensional structure than its conjugate. In Figs. 12(a) and 12(b), this trend is almost replicated, but at time $t = 7.5$ in Fig. 12(a) and time $t = 9$ in Fig. 12(b) $\Delta\mathrm{Var}_y(T)$ begins to decrease just before it becomes positive.

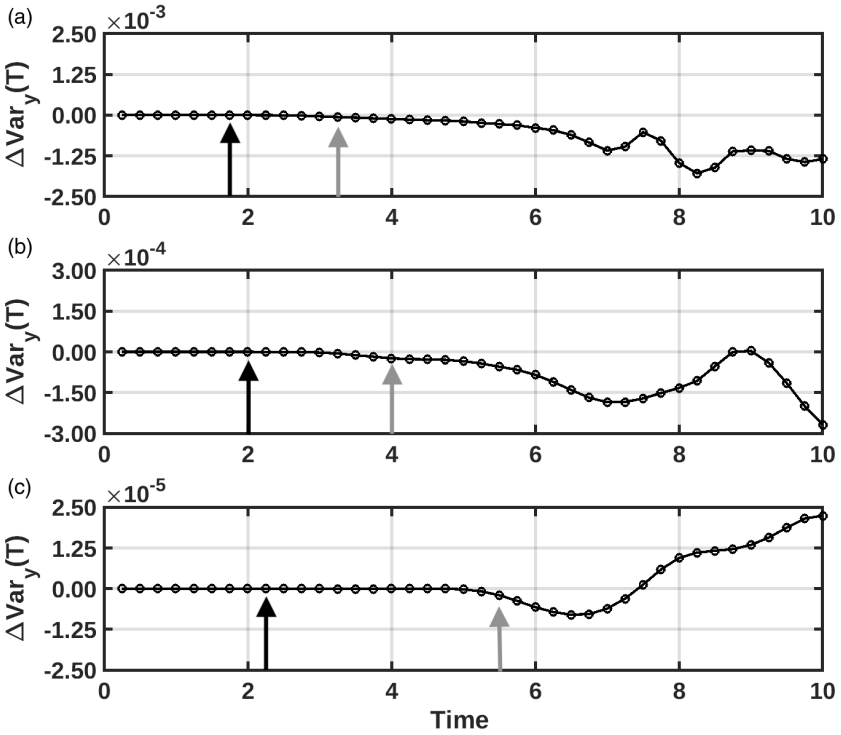

FIG. 12. The difference between the measure of spanwise variation of conjugate currents [see Eq. (36)]. Panel (a) corresponds to the B/T-High cases ($\mathrm{Gr} = 6.069 \times 10^6$), panel (b) to the B/T-Med cases ($\mathrm{Gr} = 2.146 \times 10^6$), and panel (c) to the B/T-Low cases ($\mathrm{Gr} = 7.586 \times 10^5$). For reference, the largest $\mathrm{Var}_y(T)$ of the B/T-High cases is $\mathrm{Var}_y(T) = 6.7 \times 10^{-3}$ (T-High), of the B/T-Med cases is $\mathrm{Var}_y(T) = 1.5 \times 10^{-3}$ (T-Med), and of the B/T-Low cases is $\mathrm{Var}_y(T) = 2.3 \times 10^{-4}$ (B-Low). Black arrows indicate the emergence of the lobe-cleft instability and gray arrows indicate the time when the swelling lobes begin to interact. Positive values indicate that the bottom current shows more spanwise variation, and negative values indicate the opposite.

To understand why this is the case, we must recall the following points from our discussion in Sec. III A 1:

(i) When the instability starts, the lobe-cleft structures of conjugate currents are fairly similar in shape, size, and orderliness. This is why $\Delta\mathrm{Var}_y(T) = 0$ even after the instability starts.

(ii) As the structures begin to grow, the tubes and valleys grow parallel to the streamwise axis in the B-cases, while they deviate from this parallel growth in the T-cases. This causes the first period where $\Delta\mathrm{Var}_y(T) < 0$ in Fig. 12.

(iii) The tubes and valleys of B-cases are smaller and more numerous than those of their conjugate T-cases. This means the B-case currents begin to develop more spanwise variation (to see this, count the yellow lines in Fig. 7). This leads to the first local minima in Fig. 12.

(iv) Finally, the mature lobe-cleft instability three-dimensionalizes the billows, causing them to appear as round orange/red cores surrounded by pale blue regions in Figs. 3(a)–3(e). In reality, vortex tilting/stretching generated by the baroclinic vortices of the lobe-cleft instability segment the billows (see Fig. 6). The pale blue regions reflect the fact that the segments have a large vertical offset. Furthermore, the vertical offset is greatest for T-High and T-Med currents and they therefore gain more three-dimensional structure than their conjugates. This is the source of the second period of decreasing $\Delta\mathrm{Var}_y(T)$ in Figs. 12(a) and 12(b).

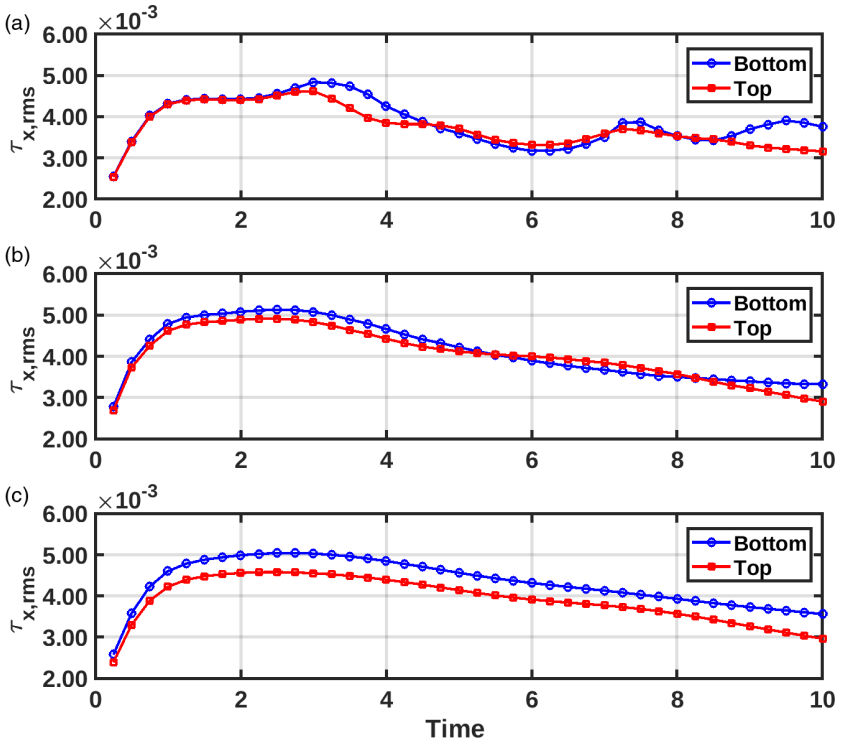

FIG. 13. The evolution of the root-mean-square (RMS) of the streamwise stress along the contact boundary. The RMS is calculated using the streamwise and spanwise average [see Eq. (37)]. Panel (a) corresponds to the $\mathrm{Gr} = 6.069 \times 10^6$ cases, panel (b) to the $\mathrm{Gr} = 2.146 \times 10^6$ cases, and panel (c) to the $\mathrm{Gr} = 7.586 \times 10^5$ cases.

The T-Low current corresponds to Fig. 3(f), and we see that it does not have billows with these pale blue regions. Its billows do not gain the associated highly three-dimensional structure, and the B/T-Low cases are therefore the only cases where we observe $\Delta \mathrm{Var}_y(T) > 0$ [see Fig. 12(c)].

2. Stress

As discussed in Sec. III B 2, the bed stresses τ_{x_i} are stresses induced along the contact boundary by a gravity current [see Eq. (18) and (17)]. They are two-dimensional fields [functions of (x, y)] and are defined along the bottom (top) boundary for bottom (top) currents. In this section we will discuss trends in the root-mean-square of the bed stresses, which are defined as follows:

$$\tau_{x_i,\,\mathrm{rms}} = \sqrt{\frac{1}{L_x L_y}\int_0^{L_y}\int_0^{L_x} \tau_{x_i}^2 dx dy}. \tag{37}$$

Streamwise stress (τ_x) is generated by the forward motion of the gravity current. As can be seen in Fig. 13, the trends in $\tau_{x,\,\mathrm{rms}}$ differ little between conjugate cases. As noted in our discussion of Fr (see Fig. 11), the discrepancy between the speed of conjugate currents decreases with Gr. This trend is reflected before time $t = 2$ in Fig. 13. The bottom current of the B/T-Low cases always generates a greater streamwise bed stress. In contrast, we see that the B/T-High currents alternate in producing a greater stress: There are roughly three periods where the bottom current produces a greater bed stress and two periods where the top produces the greater bed stress. The B/T-Med currents also alternate in producing the greatest streamwise bed stress, though there is only one period where the

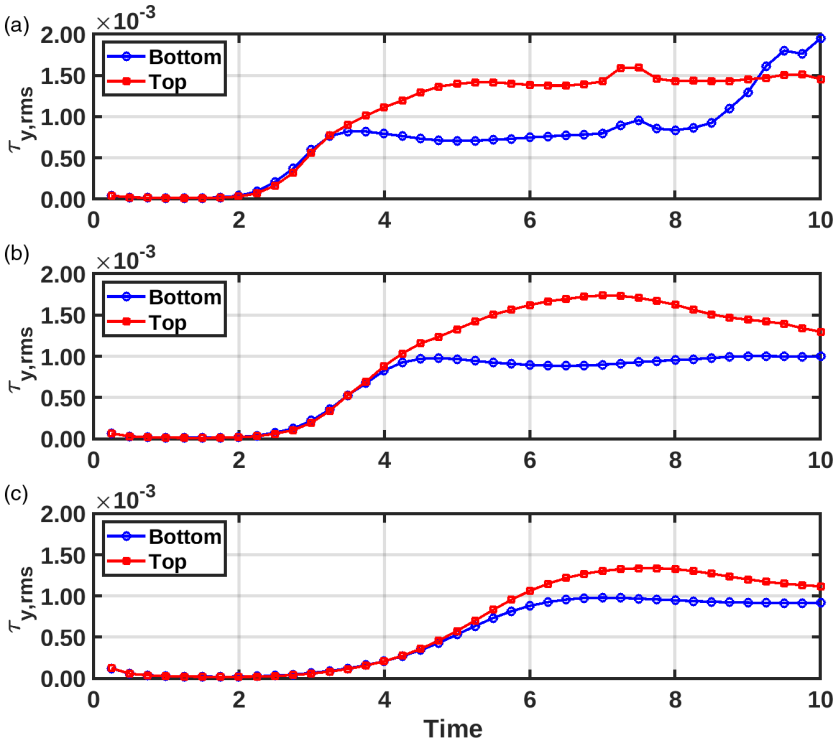

FIG. 14. Same as Fig. 13 but for the spanwise stress along the contact boundary. Note that the magnitude of the streamwise stress is approximately triple that of the the spanwise stress.

top current produces the stronger bed stress. Our proposed explanation is that individual lobes move at different speeds, and for sufficiently large Gr the fluctuations in speed among lobes increases.

Now we consider the spanwise stress, i.e., the stress on the contact boundary due to lateral motions (τ_y). Comparing the axes of Fig. 13 and Fig. 14, we see that the magnitude of the streamwise stress is approximately triple that of the spanwise stress. The weaker spanwise stress is mostly generated by the small, side-to-side motions induced by the lobe-cleft instability. We know that, initially, the spanwise stress is entirely generated by the lobe-cleft instability, because no $\tau_{y,\,\mathrm{rms}}$ signal is present before the instability initiates. The deviations in $\tau_{y,\,\mathrm{rms}}$ among conjugate currents also appear once the lobes begin to swell. The spanwise stress shows significant variation between the top and bottom cases at the same Gr, with the medium Gr currents showing the greatest disparity. In all cases, the signal of the top case is stronger than the signal of the corresponding bottom case until time $t = 9$, which implies that the lobe-cleft structures of the top currents are generating more lateral motion than those of their conjugates. As discussed in the previous subsection, the currents around the tubes are more unstable in the top cases, which explains the larger spanwise stress. After $t = 9$, the top currents of the small and medium Gr cases continue to generate a stronger spanwise stress, while the bottom current of the high Gr cases generates the stronger signal. This anomalous spike also correlated with a sharp increase in the streamwise stress of the bottom current in Fig. 13(a). Both spikes are due to the same event: The rear-most billow of the B/T-High cases impinges on the contact boundary between time $t = 8$ and $t = 10$. As can be seen in Fig. 7, the billow interacts with a larger area in the B-High case.

3. Mixing

In Fig. 15 we present the evolution of the global mixing rate [see Eq. (25)] sampled every $t = 0.25$ between $t = 0.25$ and $t = 10$. Gr increases from the bottom panel to the top panel. Initially, the

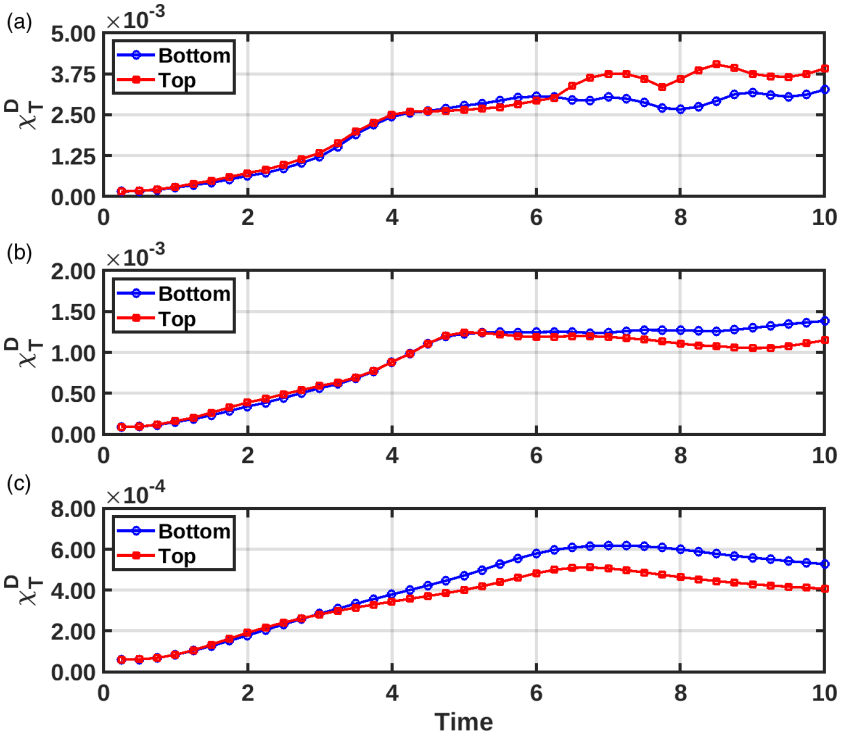

FIG. 15. Evolution of the nondimensionalized global mixing rate. Panel (a) corresponds to the Gr = 6.069×10^6 cases, panel (b) to the Gr = 2.146×10^6 cases, and panel (c) to the Gr = 7.586×10^5 cases.

global mixing rate does not differ significantly between the equivalent Gr cases, but eventually the signals diverge. In panels Figs. 15(b) and 15(c), we see that the bottom current generates the greatest mixing rates after the point of divergence. This is initially true in Fig. 15(a) (between $t = 4$ and 6), but then the mixing rate of the top current suddenly accelerates and exceeds that of the bottom current. To determine why this is the case, we need to better understand the spatial distribution of mixing. To do so, we consider $\chi_T^H(t, z)$, which is given by Eq. (26).

In each panel of Fig. 16 we present a Hovmöller plot of the difference between $\chi_T^H(t, z)$ of a bottom current and $\chi_T^H(t, L_z - z)$ of its conjugate top current [see Eq. (26) for the definition of χ_T^H]. Red regions indicate where the bottom current induces the greatest local mixing rate at a distance Δz from the contact boundary, and blue regions indicate where that is instead true of the equivalent top current. It is useful to know which current produces a greater mixing rate at a given distance from the contact boundary, since we know that the lobe-cleft instability is the dominant phenomenon near the contact boundary and that the shear-instability becomes more significant farther from the contact boundary. For this reason, we have also plotted a dashed line which indicates

$$\overline{\Delta z_N}(t) \equiv \frac{\Delta z_N^B(t) + \Delta z_N^T(t)}{2}, \tag{38}$$

where $\Delta z_N^B(t)$ is the nose height of a bottom current and $\Delta z_N^T(t)$ is the nose height of its conjugate. We can attribute phenomena far below the line to the lobe cleft instability, and we can attribute phenomena far above the line to the shear instability. This is an approximate view, of course, and we should not to preclude the possibility of one instability interfering in the domain of the other. Indeed, we have already noted that the billows of the B/T-High cases impinge on the contact boundary between $t = 7$ and $t = 10$.

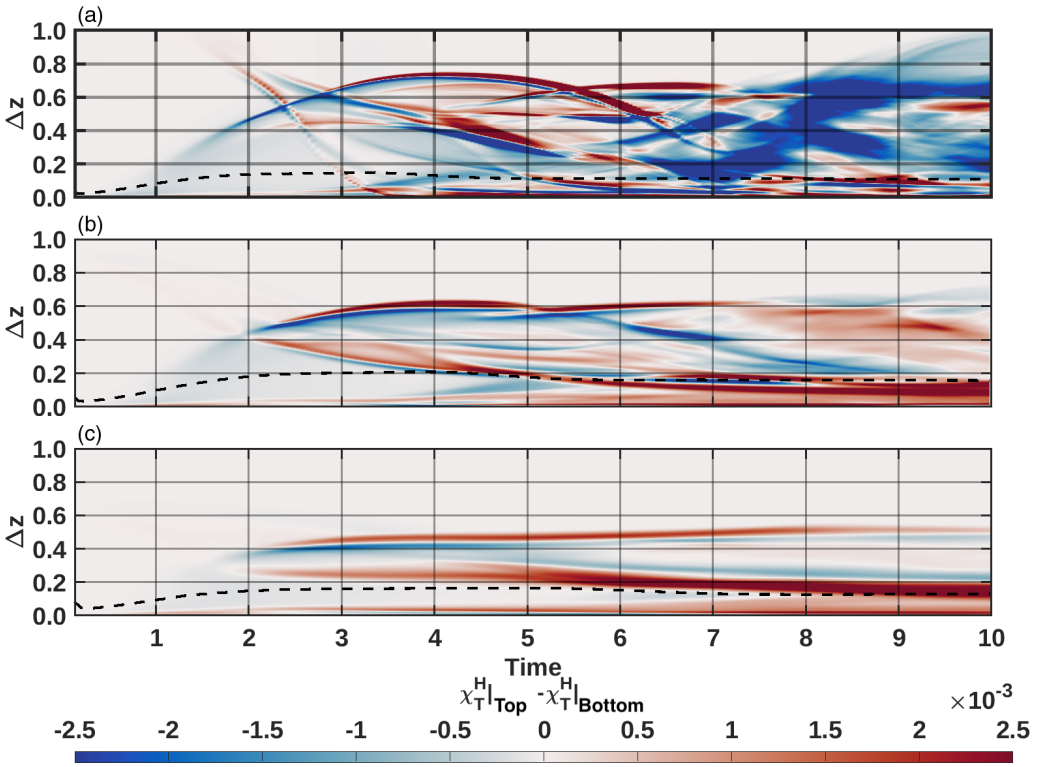

FIG. 16. The horizontally averaged local mixing rate of conjugate currents at the same Gr as a function of vertical displacement (Δz) and time (t). Panel (a) corresponds to the Gr $= 6.069 \times 10^6$ cases, panel (b) to the Gr $= 2.146 \times 10^6$ cases, and panel (c) to the Gr $= 7.586 \times 10^5$ cases. The dashed line shows $\overline{\Delta z_N}(t)$ [see Eq. (38)].

Red regions just above the contact boundary in each panel indicate that the tubes and the lower portions of the lobes and clefts of the bottom currents mix the fluid more efficiently than those of their conjugate. In Figs. 16(b) and 16(c) (which correspond to the B/T-Med and B/T-Low cases, respectively), we see red between the dashed line and the contact boundary. This indicates that the lobes, clefts, and tubes of the bottom current induce a greater mixing rate than those of its conjugate. This is not so obvious in the B/T-High cases, as we see intermittent blue and red patches below the dashed line; this is due to the aforementioned billow-contact boundary interaction.

After $t = 7$, a large blue region is present only in Fig. 16(a). As mentioned previously, the billows B/T-High, B/T-Med, and B-Low cases are segmented. The segments of the T-High current also show large amounts of vertical offset, which is not present in the other cases. The segments both increase the surface area of the current-ambient interface and decrease the width of the interface. They in turn increase $|\nabla T|^2$, and thereby the mixing rate. The enhanced vertical offset of the segments of the T-High case further thin and stretch the interface, which explains why the mixing rate of the top current exceeds that of the top current in panels Fig. 15(a) and Fig. 16(a) after $t = 6$.

As mixing is a dynamic process, we strongly urge the reader to view VIDEO-VERMIX in the Supplemental Material [48].

IV. DISCUSSION AND CONCLUSIONS

We reported on a set of numerical experiments, the results of which demonstrate the effects of weak cabbeling on three-dimensional gravity currents traveling along no-slip boundaries in

three different scenarios: high-Gr currents with tall lock-release heights; low-Gr currents with short lock-release heights; and, medium-Gr currents with intermediate lock-release heights. In agreement with two-dimensional simulations of gravity currents traveling along free-slip boundaries in the weak cabbeling regime [36], we observed that fluid ejected by the top currents travels farther from the contact boundary while bottom currents travel the fastest and farthest horizontally. We found that the B/T-Med currents traveled the farthest, the B/T-High currents the second farthest, and the B/T-Low currents the third farthest; per our discussion in Sec. II C, this is not an artifact of our nondimensionalization.

Our novel observations are concerned with the impact of weak cabbeling on the lobe-cleft instability and how it imparts three-dimensional structure onto the shear instability. Namely, we observed that top currents have fewer, larger lobes than their conjugates. We also found that the lobe-cleft instability of top currents generate more disorderly secondary instabilities than their conjugates. In other words, the tubes of top currents deviated more from their original streamwise orientation and developed a larger number of transient, unstable structures [compare Fig. 6(c) and 6(f)]. Differences in the merging processes of conjugate currents were robust across Gr. At a given lock-release height, the top current would always develop larger and fewer lobes/valleys by the end of the simulation.

Lobes are characterized by regions of alternating streamwise baroclinic vorticity, ultimately in agreement with the horseshoe vortex picture of Dai and Huang [16]. The initial streamwise density gradient generates spanwise baroclinic vorticity. As the head of the current lifts away from the contact boundary, the region between the current head and the contact boundary has an unstable stratification, which results in spanwise-varying structures that resemble—but have been argued to be distinct from—Rayleigh-Taylor instabilities [10,15,17]; in turn, these induce spanwise density gradients. The spanwise density gradients then generate streamwise baroclinic vorticity. As described by Adrian [46], the streamwise vortical currents "lift" the spanwise vortical currents; this results in the formation of hairpin/horseshoe vortices. The different initial spanwise wave number of the buoyancy-induced instability thereby determines the initial width of the horseshoe vortices and thereby the initial width of the lobes. Curiously, we notice that the initial scale of the lobe-cleft instability does not differ between conjugate currents and that differences in size do not manifest until after the lobes have begun to swell (i.e., obtain a finite width).

In the study by Grace *et al.* [36], the enhanced dissolution of top currents was interpreted as cool fluid below the temperature of maximum density being mixed more efficiently into the fluid at the temperature of maximum density than vice versa. Our results are mostly consistent with this, though the activity of lobe-cleft instabilities adds nuance. We found that currents initially mixed fluid at equal rates. However, once the lobe-cleft instability matured, the lower portion of the bottom currents gained more surface area than the equivalent region of the top currents; thus, top currents mixed fluid near the contact boundary more efficiently than their conjugates. The mature lobe-cleft instability also changed the surface area of the billows by segmenting them. This segmentation became more pronounced as Gr increases, so we eventually observed the T-High current mix the fluid more efficiently than its conjugate.

We observed that conjugate currents generate nearly equal amounts of streamwise contact bed stress. In contrast, top currents generate more spanwise stress than their conjugates due to the spurious lateral motions of their lobes and valleys. The total magnitude of the bed stress is therefore greater in the top cases. The fact that lobe-cleft structures of the bottom currents mix ambient fluid into the current more efficiently while top currents induce a greater magnitude of stress along the contact boundary begs the following question: Which current would scour the most mass from a given surface?

The longevity of cold, saline turbidity currents is an active area of investigation [23,24,49], and the nonmonoticity of the equation state for sea water (with respect to temperature [43,44]) may play a role in explaining their persistence. Namely, the reduced lateral motion of tubes and valleys paired with the large surface area they generate suggests that bottom currents are able to mix sediment into the current without losing as much TKE to friction at the solid boundary as would a top

current. That being said, we do not mean to imply that top currents are negligible in the transport of mass and heat. For instance, the lift generated by under-ice shear ejects oil droplets from the ice-water boundary [50], which implies that shear generated by top gravity currents would affect the transport of industrial waste and biofilms [51]. Furthermore, shear from under-ice currents cannot be neglected when estimating the melt rate of ice covers in winter lakes [52]. Given that top currents contribute to shear at the ice-water boundary, and given that top currents produce large stresses along the contact boundary due to spurious lateral motions of lobe-cleft structures, our work implies that models of bulk mass and heat transport must take the effects of the nonlinear equation of state into account in their estimates of the friction velocity at the ice-water boundary.

As noted in Sec. III, none of the systems entered the inertial or viscous phases. Future work should extend the lengths of the domain so that these phases are accessed, as information about weak cabbeling in these phases will be relevant at the field scale. We estimate that differences in the three-dimensional structures will still be observed, as top and bottom currents will enter the inertial phase with different x_N and u_c due to accumulated deviations during the slumping phase.

While the shape, speed, mixing, and stresses of the currents differ between top and bottom currents, they both contribute significantly to hydrological processes where they arise. While we have focused on the effects of nonlinearity in the freshwater equation of state, the nonlinearity in temperature persists even when accounting for dissolved mass [43,44]. Consequently, interesting and surprising results related to nonlinear equations of state must also exist in oceanographic and lacustrine systems and therefore warrant further investigation.

ACKNOWLEDGMENTS

This research project was funded by the Natural Sciences and Engineering Research Council of Canada (NSERC) Discovery Grant No. RGPIN-311844-37157. We thank the anonymous referees for the constructive comments that improved our paper.

[1] J. E. Simpson, Gravity currents in the laboratory, atmosphere, and ocean, Annu. Rev. Fluid Mech. **14**, 213 (1982).
[2] H. E. Huppert, Gravity currents: a personal perspective, J. Fluid Mech. **554**, 299 (2006).
[3] J. E. Simpson, *Gravity Currents: In the Environment and the Laboratory* (Cambridge University Press, Cambridge, UK, 1999).
[4] A. R. Horner-Devine and C. C. Chickadel, Lobe-cleft instability in the buoyant gravity current generated by estuarine outflow, Geophys. Res. Lett. **44**, 5001 (2017).
[5] M. O. Baringer and J. F. Price, Mixing and spreading of the mediterranean outflow, J. Phys. Oceanogr. **27**, 1654 (1997).
[6] J. Charba, Application of gravity current model to analysis of squall-line gust front, Mon. Weather Rev. **102**, 140 (1974).
[7] R. S. J. Sparks, J. Barclay, E. S. Calder, R. A. Herd, J.-C. Komorowski, R. Luckett, G. E. Norton, L. J. Ritchie, B. Voight, and A. W. Woods, Generation of a debris avalanche and violent pyroclastic density current on 26 December (Boxing Day) 1997 at Soufrière Hills Volcano, Montserrat, Geol. Soc. Lond. Mem. **21**, 409 (2002).
[8] T. von Kármán, The engineer grapples with nonlinear problems, Bull. Am. Math. Soc. **46**, 615 (1940).
[9] T. B. Benjamin, Gravity currents and related phenomena, J. Fluid Mech. **31**, 209 (1968).
[10] J. E. Simpson, Effects of the lower boundary on the head of a gravity current, J. Fluid Mech. **53**, 759 (1972).
[11] R. E. Britter and J. E. Simpson, Experiments on the dynamics of a gravity current head, J. Fluid Mech. **88**, 223 (1978).
[12] H. E. Huppert and J. E. Simpson, The slumping of gravity currents, J. Fluid Mech. **99**, 785 (1980).

[13] J. W. Rottman and J. E. Simpson, Gravity currents produced by instantaneous releases of a heavy fluid in a rectangular channel, J. Fluid Mech. **135**, 95 (1983).
[14] T. H. Ellison, Meteorology, Sci. Progress (1933-) **49**, 57 (1961).
[15] C. Härtel, F. Carlsson, and M. Thunblom, Analysis and direct numerical simulation of the flow at a gravity-current head. Part 2. The lobe-and-cleft instability, J. Fluid Mech. **418**, 213 (2000).
[16] A. Dai and Y.-L. Huang, On the merging and splitting processes in the lobe-and-cleft structure at a gravity current head, J. Fluid Mech. **930**, A6 (2022).
[17] C. Härtel, E. Meiburg, and F. Necker, Analysis and direct numerical simulation of the flow at a gravity-current head. Part 1. Flow topology and front speed for slip and no-slip boundaries, J. Fluid Mech. **418**, 189 (2000).
[18] M. I. Cantero, S. Balachandar, M. H. García, and J. P. Ferry, Direct numerical simulations of planar and cylindrical density currents, J. Appl. Mech. **73**, 923 (2006).
[19] M. I. Cantero, J. R. Lee, S. Balachandar, and M. H. Garcia, On the front velocity of gravity currents, J. Fluid Mech. **586**, 1 (2007).
[20] M. I. Cantero, S. Balachandar, M. H. García, and D. Bock, Turbulent structures in planar gravity currents and their influence on the flow dynamics, J. Geophys. Res. **113**, C08018 (2008).
[21] H. E. Huppert, Flow and instability of a viscous current down a slope, Nature (Lond.) **300**, 427 (1982).
[22] A. Jackson, B. Turnbull, and R. Munro, Scaling for lobe and cleft patterns in particle-laden gravity currents, Nonlin. Process. Geophys. **20**, 121 (2013).
[23] E. Meiburg and B. Kneller, Turbidity currents and their deposits, Annu. Rev. Fluid Mech. **42**, 135 (2010).
[24] E. Meiburg, S. Radhakrishnan, and M. Nasr-Azadani, Modeling gravity and turbidity currents: Computational approaches and challenges, Appl. Mech. Rev. **67**, 040802 (2015).
[25] M. G. Wells and R. M. Dorrell, Turbulence processes within turbidity currents, Annu. Rev. Fluid Mech. **53**, 59 (2021).
[26] B. C. Kneller, S. J. Bennett, and W. D. McCaffrey, Velocity structure, turbulence and fluid stresses in experimental gravity currents, J. Geophys. Res.: Oceans **104**, 5381 (1999).
[27] K. Bhaganagar, Role of head of turbulent 3-D density currents in mixing during slumping regime, Phys. Fluids **29**, 020703 (2017).
[28] M. I. Cantero, A. Cantelli, C. Pirmez, S. Balachandar, D. Mohrig, T. A. Hickson, T.-h. Yeh, H. Naruse, and G. Parker, Emplacement of massive turbidites linked to extinction of turbulence in turbidity currents, Nat. Geosci. **5**, 42 (2012).
[29] J. D. Parsons, W. J. Schweller, C. W. Stelting, J. B. Southard, W. J. Lyons, and J. P. Grotzinger, A preliminary experimental study of turbidite fan deposits, J. Sediment. Res. **72**, 619 (2002).
[30] G. Kirillin, M. Leppäranta, A. Terzhevik, N. Granin, J. Bernhardt, C. Engelhardt, T. Efremova, S. Golosov, N. Palshin, P. Sherstyankin, G. Zdorovennova, and R. Zdorovennov, Physics of seasonally ice-covered lakes: a review, Aquat. Sci. **74**, 659 (2012).
[31] D. Bouffard and A. Wüest, Convection in lakes, Annu. Rev. Fluid Mech. **51**, 189 (2019).
[32] C. L. Ramón, H. N. Ulloa, T. Doda, K. B. Winters, and D. Bouffard, Bathymetry and latitude modify lake warming under ice, Hydrol. Earth Syst. Sci. **25**, 1813 (2021).
[33] T. Doda, C. L. Ramón, H. N. Ulloa, A. Wüest, and D. Bouffard, Seasonality of density currents induced by differential cooling, Hydrol. Earth Syst. Sci. **26**, 331 (2022).
[34] J. Jansen, S. MacIntyre, D. C. Barrett, Y.-P. Chin, A. Cortés, A. L. Forrest, A. R. Hrycik, R. Martin, B. C. McMeans, M. Rautio, and R. Schwefel, Winter limnology: How do hydrodynamics and biogeochemistry shape ecosystems under ice? J. Geophys. Res.:Biogeosciences **126**, e2020JG006237 (2021).
[35] K. D. Stewart, T. W. Haine, A. M. Hogg, and F. Roquet, On cabbeling and thermobaricity in the surface mixed layer, J. Phys. Oceanogr. **47**, 1775 (2017).
[36] A. P. Grace, M. Stastna, K. G. Lamb, and K. A. Scott, Asymmetries in gravity currents attributed to the nonlinear equation of state, J. Fluid Mech. **915**, A18 (2021).
[37] K. Bhaganagar, Direct numerical simulation of lock-exchange density currents over the rough wall in slumping phase, J. Hydraul. Res. **52**, 386 (2014).
[38] A. Ghassemi, S. Zahedi, and L. Boegman, Bolus formation from fission of nonlinear internal waves over a mild slope, J. Fluid Mech. **932**, A50 (2022).

[39] A. P. Grace, M. Stastna, K. G. Lamb, and K. A. Scott, Gravity currents in the cabbeling regime, Phys. Rev. Fluids **8**, 014502 (2023).
[40] C. J. Subich, K. G. Lamb, and M. Stastna, Simulation of the Navier–Stokes equations in three dimensions with a spectral collocation method, Int. J. Numer. Methods Fluids **73**, 103 (2013).
[41] P. F. Kundu and I. M. Cohen, *Fluid Mechanics, 4th ed.* (Elsevier, Amsterdam, 2004).
[42] J. Olsthoorn, E. W. Tedford, and G. A. Lawrence, Diffused-interface Rayleigh-Taylor instability with a nonlinear equation of state, Phys. Rev. Fluids **4**, 094501 (2019).
[43] T. J. McDougall, D. R. Jackett, D. G. Wright, and R. Feistel, Accurate and computationally efficient algorithms for potential temperature and density of seawater, J. Atmos. Ocean. Technol. **20**, 730 (2003).
[44] D. Brydon, S. Sun, and R. Bleck, A new approximation of the equation of state for seawater, suitable for numerical ocean models, J. Geophys. Res. **104**, 2156 (1999).
[45] J. C. Wyngaard, *Turbulence in the Atmosphere* (Cambridge University Press, Cambridge, UK, 2010).
[46] R. J. Adrian, Hairpin vortex organization in wall turbulence, Phys. Fluids **19**, 041301 (2007).
[47] N. Didden and T. Maxworthy, The viscous spreading of plane and axisymmetric gravity currents, J. Fluid Mech. **121**, 27 (1982).
[48] See Supplemental Material at http://link.aps.org/supplemental/10.1103/PhysRevFluids.8.113901 for movies depicting the evolution of the salinity and density fields.
[49] S. Fukuda, M. G. W. de Vet, E. W. G. Skevington, E. Bastianon, R. Fernández, X. Wu, W. D. McCaffrey, H. Naruse, D. R. Parsons, and R. M. Dorrell, Inadequacy of fluvial energetics for describing gravity current autosuspension, Nat. Commun. **14**, 2288 (2023).
[50] M. C. Boufadel, F. Cui, J. Katz, T. Nedwed, and K. Lee, On the transport and modeling of dispersed oil under ice, Mar. Pollut. Bull. **135**, 569 (2018).
[51] M. Salta, J. A. Wharton, Y. Blache, K. R. Stokes, and J.-F. Briand, Marine biofilms on artificial surfaces: structure and dynamics, Environ. Microbiol. **15**, 2879 (2013).
[52] G. Kirillin, I. Aslamov, V. Kozlov, R. Zdorovennov, and N. Granin, Turbulence in the stratified boundary layer under ice: observations from Lake Baikal and a new similarity model, Hydrol. Earth Syst. Sci. **24**, 1691 (2020).